

Review

A Review of Recent Research on Flow and Heat Transfer Analysis in Additively Manufactured Transpiration Cooling for Gas Turbines

Kirttayoth Yeranee ¹ and Yu Rao ^{1,2,*}

¹ Institute of Turbomachinery, School of Mechanical Engineering, Shanghai Jiao Tong University, Shanghai 200240, China; krittayoch.y@gmail.com

² Shenzhen Research Institute, Shanghai Jiao Tong University, Shenzhen 518000, China

* Correspondence: yurao@sjtu.edu.cn

Abstract

Advanced gas turbine cooling technologies are required to bridge the gap between turbine inlet temperatures and component thermal limits. Transpiration cooling has emerged as a promising method, leveraging porous structures to enhance cooling effectiveness. Recent advancements in additive manufacturing (AM) enable precise fabrication of complex transpiration cooling architectures, such as triply periodic minimal surface (TPMS) and biomimetic designs. This review analyzes AM-enabled transpiration cooling for gas turbines, elucidating key parameters, heat transfer mechanisms, and flow characteristics of AM-fabricated designs through experimental and numerical studies. Previous research has concluded that well-designed transpiration cooling achieves cooling effectiveness up to five times higher than the traditional film cooling methods, minimizes jet lift-off, improves temperature uniformity, and reduces coolant requirements. Optimized coolant controls, graded porosity designs, complex topologies, and hybrid cooling architectures further enhance the flow uniformity and cooling effectiveness in AM transpiration cooling. However, challenges remain, including 4–77% porosity shrinkage in perforated transpiration cooling for 0.5–0.06 mm holes, 15% permeability loss from defects, and 10% strength reduction in AM models. Emerging solutions include experimental validations using advanced diagnostics, high-fidelity multiphysics simulations, AI-driven and topology optimizations, and novel AM techniques, which aim at revolutionizing transpiration cooling for next-generation gas turbines operating under extreme conditions.



Academic Editors: Andrzej Frąckowiak, Bartosz Ciupek and Łukasz Brodzik

Received: 12 May 2025

Revised: 13 June 2025

Accepted: 21 June 2025

Published: 23 June 2025

Citation: Yeranee, K.; Rao, Y. A Review of Recent Research on Flow and Heat Transfer Analysis in Additively Manufactured Transpiration Cooling for Gas Turbines. *Energies* **2025**, *18*, 3282. <https://doi.org/10.3390/en18133282>

Copyright: © 2025 by the authors. Licensee MDPI, Basel, Switzerland. This article is an open access article distributed under the terms and conditions of the Creative Commons Attribution (CC BY) license (<https://creativecommons.org/licenses/by/4.0/>).

Keywords: additive manufacturing; gas turbine cooling; heat transfer analysis; transpiration cooling

1. Introduction

1.1. Importance of Advanced Cooling Technology for Gas Turbines

Gas turbines are widely used in aviation and power generation due to their high power density, efficiency, and performance. The global market of gas turbines is projected to grow further due to technological advancements and the shift toward distributed power generation. Performance improvements are motivated by the purpose of decreasing fuel consumption, saving subsequent expenses, and reducing carbon dioxide (CO₂) emissions. According to the Brayton cycle, increasing turbine inlet temperature (TIT) is the most effective way to enhance performance [1], as shown in Figure 1a [2]. Modern combined-

cycle plants with 1700 °C-class turbines achieve around 65% efficiency [3], while aero-engines will operate at TITs exceeding 1800 °C. Heavy-duty turbines, such as Mitsubishi's M701J, have reached 1600 °C, with future designs targeting 1700 °C [4].

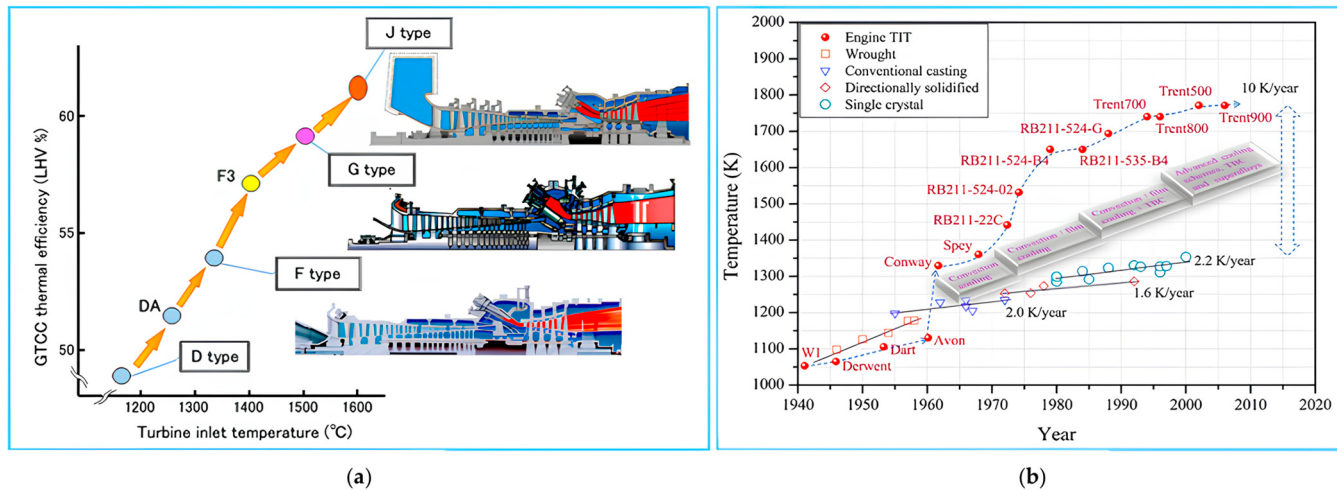


Figure 1. Development in gas turbine: (a) TIT effects on gas turbine power and effectiveness and (b) Evolution of temperature capabilities of materials and thermal barrier coatings (These figures are reproduced from [2,5] under a Creative Commons Attribution (CC BY) license).

Despite these advancements, material limitations remain a critical challenge. Modern superalloys and thermal barrier coatings (TBCs) allow turbine blades to withstand temperatures around 1300 °C [6,7], as depicted in Figure 1b [5]; however, combustor temperatures are projected to exceed 1800 °C to obtain higher efficiency and power output. Furthermore, the maximum temperature for superalloys increases at a rate of only 8 °C per year, whereas the TITs are growing by up to 20 °C annually. To bridge this gap, advanced cooling technologies must be implemented to protect turbine components from thermal failure under these extreme operating conditions.

1.2. Evolution from Traditional to Transpiration Cooling

The evolution of gas turbine cooling has progressed from simple convection cooling to advanced transpiration cooling, with each stage improving cooling effectiveness, as shown in Figure 2. Early convection cooling was enhanced through various methods, including rib turbulators [8], pin fins [9], and protrusions/dimples [10]. Impingement cooling subsequently emerged as a high-performance alternative due to its superior heat transfer enhancement (Nu/Nu_0) [11,12]. However, internal cooling schemes, even combined ones, such as pin fin-dimple or rib-dimple, leave blade surfaces exposed to hot gas and cannot meet thermal protection requirements. This limitation led to the development of external cooling, i.e., film cooling, which forms a protective layer over the surface to improve cooling effectiveness. Many researchers have developed various techniques to enhance its efficiency [13]. As hole density increases, film cooling transitions to effusion cooling, which provides a full-coverage film layer to hot surfaces.

Impingement/effusion cooling, also known as double-wall cooling, has been used to improve gas turbine thermal protection since the 1980s [14,15]. This scheme combines the advantages of jet impingement and film cooling through a perforated wall with supporting structures. Studies have shown that double-wall cooling achieves higher cooling effectiveness than other conventional cooling methods, with pedestals improving heat transfer uniformity [16–19]. However, careful design is required to avoid performance degradation. The double-wall cooling system has also faced durability challenges from thermal stresses between layers. Skamniotis et al. [20–22] revealed that reducing hole ellipticity and opti-

mizing pedestal spacing can mitigate stresses. Courtis et al. [23] showed that optimized hole spacing, particularly in the spanwise direction, can achieve film effectiveness up to 0.9, whereas increased porosity (φ) reduces mechanical strength, necessitating careful thermomechanical design trade-offs for practical implementation.

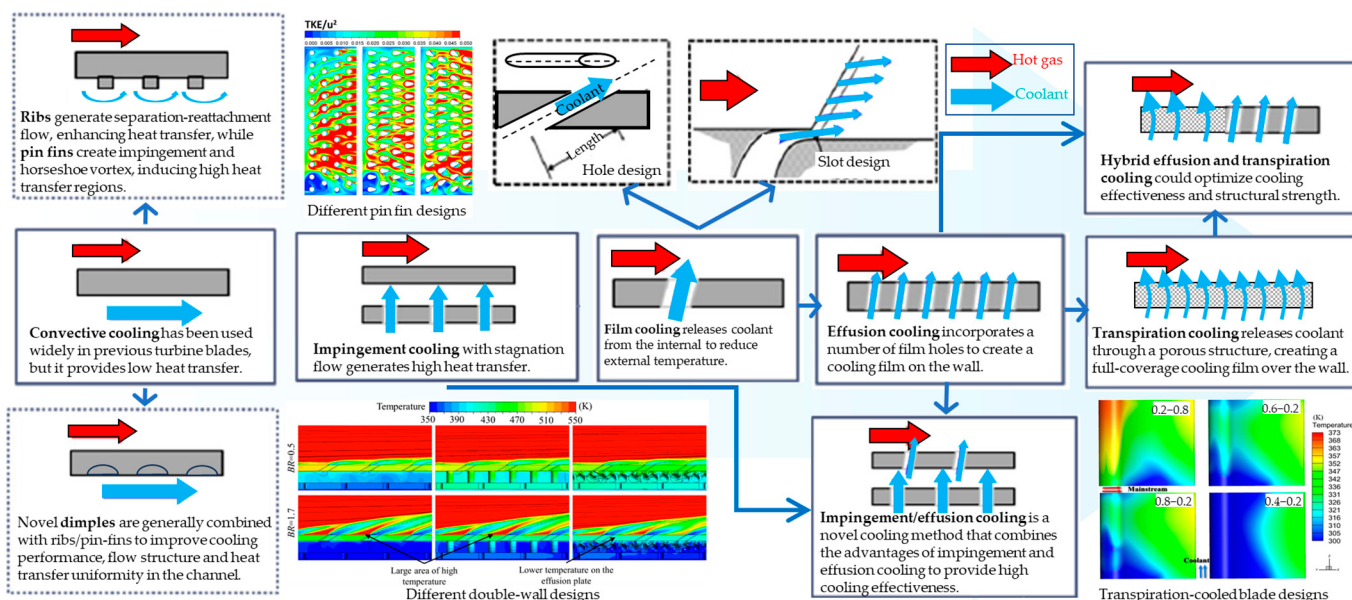


Figure 2. Overview of advanced cooling methods for gas turbine blades. Different pin fin designs, reproduced with permission from [24]. Copyright 2021 Elsevier, Different double-wall designs, reproduced with permission from [18]. Copyright 2021 Elsevier, Transpiration-cooled blade designs, reproduced with permission from [25]. Copyright 2023 Elsevier.

To balance film coverage uniformity with mechanical strength, transpiration cooling systems can be integrated with film holes [26,27]. However, conventional porous-media-based transpiration materials, such as metal foams, sintered particles, and woven meshes, lack the structural integrity required for turbine blade applications. While porous transpiration cooling has demonstrated high efficiency in rocket engines [28] and has since been adapted for gas turbines [29,30], scramjets [31], and high-speed vehicles [32], ongoing research focuses on novel materials [33], alternative coolants [34], and heat transfer enhancement techniques [35]. Additive manufacturing (AM) offers a promising solution by enabling precise and high-performance cooling designs [2]. Despite its potential, the flow and heat transfer analysis of AM-fabricated transpiration cooling remains underexplored in the existing literature [5,36–46].

1.3. Framework and Objectives

Given the urgent demand for high-performance cooling in gas turbines and the rapid advancements in AM technology, there is a critical need for a comprehensive framework that integrates both domains. This article presents a review of recent research on flow and heat transfer analysis in additively manufactured transpiration cooling systems for gas turbines, which is structured into six key sections. First, the significance and evolution of gas turbine cooling are introduced. The Section 2 summarizes the literature review of transpiration cooling, including research progress and its classification. The development of AM techniques tailored for transpiration cooling applications is then presented in the Section 3. The Section 4 analyzes flow and heat transfer characteristics in AM transpiration cooling, drawing insights from recent experimental and numerical studies, as well as

optimization efforts. The Section 5 addresses challenges and future directions. Finally, the paper concludes by summarizing the main findings and their implications.

2. Literature Review of Transpiration Cooling

2.1. Research Progress and Challenges of Transpiration Cooling

The prior review articles on transpiration cooling have been widely established, mainly for aerospace and high-speed vehicles. Figure 3 summarizes the benefits, existing key challenges, and solutions, highlighting its implementation feasibility for gas turbines and high-speed vehicles. Most reviews [5,36–46] affirmed that transpiration cooling held significant promise for these applications due to high cooling performance, customizable design, and enhanced surface protection. Advances in AM technology enabled the fabrication of precision micro and transpiration cooling structures, addressing critical challenges such as particle-induced clogging, mechanical integrity, and manufacturing limitations. Additionally, research on hybrid cooling methods has been advancing, aiming to enhance thermomechanical performance under extreme conditions.

Transpiration cooling		Key challenges	
Solutions		Gas turbines	Aerospace/high-speed vehicles
<ul style="list-style-type: none"> High performance: maintains safe temperature in extreme conditions, outperforming effusion and double-wall cooling. Customizable designs Enhanced protection: better deflection of large particles for liquid-cooled blades. 		<ul style="list-style-type: none"> Limited data: mixing losses, particle-flow interactions, heat transfer, erosion, and roughness for optimal design. Purity needs: requires ultra-clean coolant-mainstream flow to avoid clogging. High costs: more expensive than effusion, Lamilloy, or Transply cooling methods. Precision-dependent: needs carefully controlled porous walls for uniform cooling. Technical hurdles: material/processing limits, unresolved thermal-fluid complexities, and durability concerns. 	<ul style="list-style-type: none"> Material demands: requires advanced porous materials balancing oxidation resistance, strength, and permeability. Phase-change issues: vapor blockage, thermal oscillations, and heat transfer degradation. Design unknowns: poorly understood film-mainstream interaction, downstream coverage mechanisms, pyrolysis, and coking effects. System integration: lacks coupling mechanisms and engine-cooling performance validation. Research shortfalls: insufficient high-resolution data/simulations on phase change in porous media.
<ul style="list-style-type: none"> Advanced AM technology: enables high precision-engineered for high-performance transpiration cooling structures with superior mechanical properties. Hybrid cooling : integrates transpiration cooling with other methods for lightweight, cost-efficient, and multifunctional designs. Validation: high-resolution testing and advanced thermal/flow analysis ensure optimized performance. 		<ul style="list-style-type: none"> AM Limitations: material and post-processing constraints hinder high-accuracy fabrication. Performance Gaps: needs better porosity control, thermal fatigue resistance, and scalable manufacturing for optimized heat transfer and pressure distribution. Validation: requires experimental validations and precision printing, especially sub-50 µm structures. 	

Figure 3. Summary of prior review articles on transpiration cooling techniques.

While existing reviews have thoroughly documented conventional transpiration cooling approaches, they identified critical knowledge gaps, especially in AM technology for transpiration cooling structures, experimental/numerical studies on AM-fabricated transpiration cooling systems, and detailed flow/heat transfer analysis for gas turbines. This review, therefore, addresses these gaps by evaluating recent advances in AM techniques, experimental and computational results, and optimized transpiration cooling studies, providing a comprehensive framework for implementing AM transpiration cooling in next-generation gas turbines.

2.2. Classification of Transpiration Cooling

In previous studies, transpiration cooling is also called sweat [47], effusion [48], or full-coverage film cooling [49]. Therefore, it is essential to understand the classification of transpiration cooling, as this framework defines the cooling capacity, material requirement, and manufacturing effect that guide design and performance evaluation. Transpiration cooling employs three primary mechanisms, classified based on working conditions, as summarized in Figure 4 [44]: solid cooling using phase-changing metals for passive heat absorption [50], gas cooling via forced flow through porous structures [49,51], and liquid cooling combining passive and active methods with phase-change enhancement [52–54].

The passive approach relies on material vaporization, while forced methods create protective coolant boundary layers through porous media.

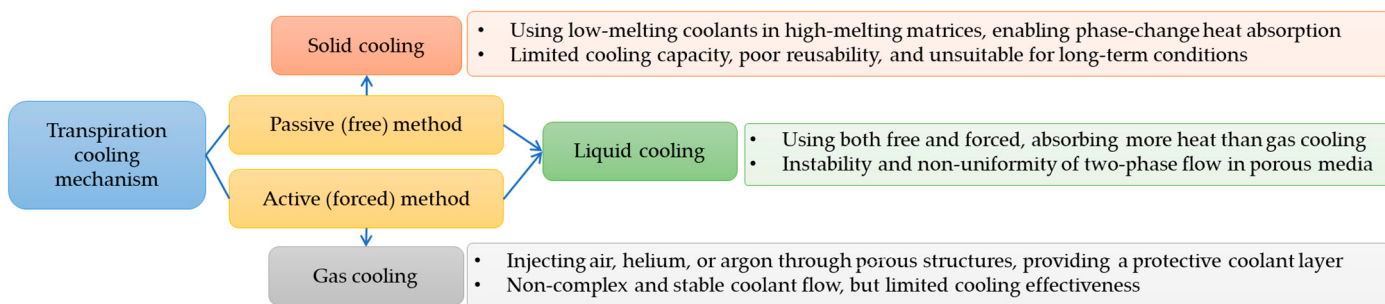


Figure 4. Classification of transpiration cooling based on working conditions.

Hypersonic vehicles and rocket engines operating above 2000 °C can achieve remarkable cooling capacities approaching 1000 MW/m² through liquid transpiration with phase-change enhancement [55]. Meanwhile, aero-engine turbines are limited to 50–100 MW/m² when using compressor bleed air through effusion or transpiration cooling, which are also constrained by the temperature limits of superalloys and ceramic matrix composites (CMCs) below 1500 °C. Moreover, liquid transpiration cooling systems, especially in gas turbines, could cause high thermal stress and pore clogging during rapid phase changes.

The current gas-phase (also known as single-phase) transpiration cooling is the most suitable for current gas turbines. The gas-phase transpiration cooling materials can be further categorized into porous media and laminated materials [38]. The porous-media transpiration materials include a metal-based type fabricated through powder sintering or advanced AM techniques and a ceramic-based type, which offers superior high-temperature performance [56]. However, sintered porous materials suffer from limited high-temperature oxidation resistance and structural strength. Meanwhile, ceramic-based transpiration faces brittleness and incompatibility with other metal structures in current technology, even though the ceramic material demonstrates excellent thermal stability and reduced coolant requirements [57].

On the other hand, laminated materials, traditionally constrained by manufacturing complexity and thermal limitations [58], have benefited from recent advances in AM technology [59–62]. Innovative approaches such as gradient laser sintering of 316 L stainless steel have enabled precise pore structure control, significantly improving anti-blockage performance and cooling efficiency [63]. Metal material with gradient φ has successfully been fabricated through the utilization of the selective laser melting (SLM) technique, in which a gradient-changing scan speed is incorporated in each SLM layer [64]. The smoothly graded pore structures are fabricated using this AM technology, resulting in optimized coolant distribution, which minimizes pore clogging and enhances cooling performance. As a result, metal-based type transpiration cooling is more viable for gas turbines when implemented in precisely engineered and non-stochastic architectures fabricated through advanced AM techniques. The following sections explore the role of AM in transpiration cooling and current flow/heat transfer analysis to address gaps identified in prior studies [5,36–46].

3. Additive Manufacturing for Transpiration Cooling

3.1. Traditional Manufacturing for Transpiration Cooling

Manufacturing developments of transpiration cooling for high-speed vehicles have been well documented in previous work [38,44,45], concluding that metal-based transpiration materials have been traditionally fabricated by powder sintering, fiber sintering,

and melt casting, including bronze, stainless steel, titanium, and alloys. Powder-sintered porous metals, such as copper-based cooling systems by NASA [65], have been used in rocket engines. Recent advancements, such as metal powder injection molding (MIM), enabled precise control over pore geometry, allowing complex structures, such as inclined porous struts, for hybrid film/transpiration cooling [26]. Additionally, conventional laminated cooling fabrication involved etching or laser-cutting micro-cooling channels into thin metal sheets, followed by layer stacking and welding [66]. However, this method was time-consuming, limited to specific metals, and incapable of achieving precise complex micro-channel geometries, restricting its overall effectiveness. Therefore, the AM technique is essential to overcome the limitations of the traditional methods for efficiently fabricating advanced transpiration cooling structures for gas turbines.

3.2. Additive Manufacturing Techniques for Transpiration Cooling

Compared to conventional fabrication methods, the AM technology has offered higher precision by combining computer-aided design (CAD) with minimized material consumption and increased production efficiency. The AM allows full control over pore shape and size, making it ideal for complex designs, such as gas turbine blades with advanced cooling channels. Figure 5 shows the topology-optimized trailing edge (TE) on the scale of a gas turbine blade [67]. This study has concluded that the SLM method provided accurate printing with no micro-voids, staircase effects, or partially melted particles, and post-processing ensured a smooth external surface. Another notable example is Siemens's application of direct metal laser sintering (DMLS), developed by Electro Optical Systems (EOS), Germany, to fabricate turbine blades with optimized internal cooling structures, demonstrating the capability of the AM technology for high-performance complex cooling channels in gas turbines [68].

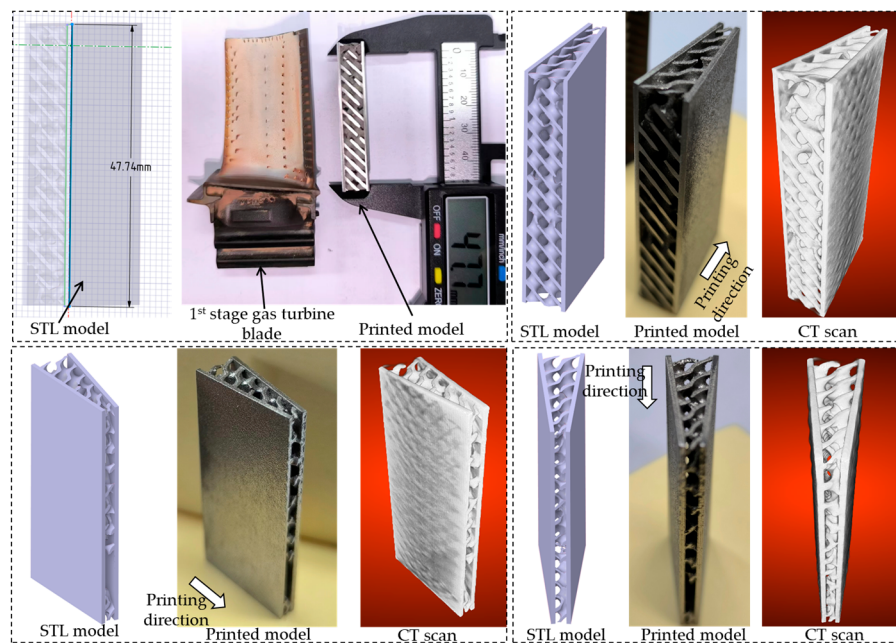


Figure 5. Complex gas turbine cooling structures fabricated using the SLM method. Reproduced with permission from [67]. Copyright 2024 Elsevier.

Three metal AM methods have emerged as key technologies for gas turbine applications, including powder bed binder jetting [69], direct laser deposition (DLD) [70], and laser powder bed fusion (LPBF) [71] for both full melt (laser melting) and partial melt (laser sintering). Each method offers distinct advantages and limitations, leading to different use cases in gas turbine component fabrication. Figure 6 summarizes the working prin-

ciples, advantages, and drawbacks of these AM techniques in the context of gas turbine manufacturing [72].

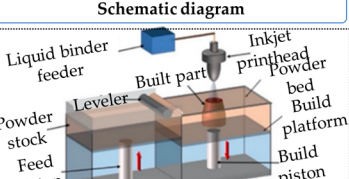
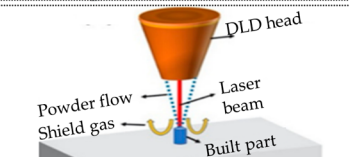
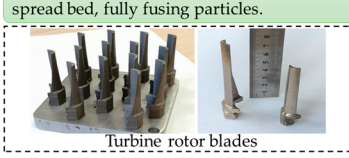
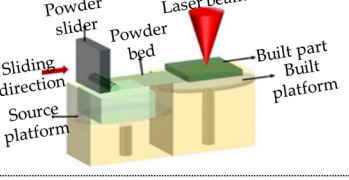
	Principles and examples of built parts	Schematic diagram	Advantages	Limitations
Binder jetting	A liquid binder is selectively jetted onto a powder bed to bond particles layer by layer. 		<ul style="list-style-type: none"> High production speed compared to LPBF Scalability for mass production More cost effective than LPBF 	<ul style="list-style-type: none"> Impurities, affecting high-temperature performance Lower mechanical properties Requiring careful dimensional compensation due to shrinkage in the sintering process Less established than LPBF for turbine blades
DLD	A laser melts powder as it is deposited, building the part layer by layer. 		<ul style="list-style-type: none"> High deposition rates and large-scale builds Minimal waste and cost-effective repairs No support structures needed 	<ul style="list-style-type: none"> Lower resolution and surface finish Requiring stress-relief heat treatments Limited geometric complexity, such as lattices Requiring CNC machining, polishing and heat treatment
LPBF	A laser selectively melts the powder in a pre-spread bed, fully fusing particles. 		<ul style="list-style-type: none"> High precision for complex geometries Excellent material properties Ideal for expensive superalloys Enables custom designs 	<ul style="list-style-type: none"> Higher cost and slower build rates than other methods Requiring stress-relief heat treatments Restricted by powder bed size Requiring supports for overhangs

Figure 6. A summary of AM techniques for gas turbines. Lattice structures, reproduced with permission from [69]. Copyright 2022 Elsevier. Damaged and repaired blades, reproduced with permission from [70]. Copyright 2014 Elsevier. Turbine rotor blades, reproduced with permission from [71]. Copyright 2020 Elsevier. The schematic diagrams are reproduced from [72] under a Creative Commons Attribution (CC BY) license.

Most of the transpiration-cooling designs for gas turbine research have been successfully fabricated using the LPBF method, enabling detailed flow/heat transfer and structural analysis. Key studies are shown in Table 1. These studies demonstrated that the LPBF method allowed the fabrication of highly complex transpiration-cooling designs with robust mechanical properties and superior cooling performance. This represents a transformative advancement for next-generation gas turbine cooling technologies.

Table 1. Examples of metal AM-fabricated transpiration-cooling designs for gas turbine research.

Ref.	Material	Key Design/Feature	Significance
[73]		Porous media on a C3X single-turbine blade	Pioneering transpiration cooling for validating the feasibility of turbine blades
[30]		and cascade turbine blades	
[66]		0.24 mm perforated holes	Achieving a tight tolerance with only a 4% φ deviation compared to the design
[74]	Hastelloy-X	Porous-media transpiration cooling	Verifying the high-temperature material compatibility
[75]		Optimized LPBF parameters for porous media	Obtaining controlled pores and accurate φ for various transpiration-cooled plates
[76]		Innovative hole topology designs	Paving the way for new research on AM-hole topology to improve cooling effectiveness and uniformity
[77]		0.2 mm perforated holes	Capable of fabricating ultra-fine holes, providing high cooling efficiencies, and desired tensile strength
[78]	Inconel 718	Perforated holes with internal lattices	Groundbreaking research on minimizing crossflow effects in AM transpiration-cooled plates
[51]		Reinforcement for transpiration cooling	Improving mechanical integrity with a minor loss in cooling performance
[79]		Double-cavity leading edge (LE) cooling	Demonstrating advanced, complex internal and external cooling structures
[80]	Inconel 625	Gyroid TPMS-based transpiration cooling	Novel lattice design with high temperature and corrosion resistance

3.3. Additive Manufacturing-Fabricated Advanced Transpiration Cooling Structures

Advancements in AM technology have enabled the fabrication of complex and high-performance transpiration cooling structures for gas turbines, offering superior thermal management compared to conventional cooling techniques [2,46]. These structures can be categorized according to porosity control into stochastic [73–75] and deterministic structures [77,78,80–83], as shown in Figure 7. The random-pore distributions usually caused uncontrolled flow paths, limited cooling uniformity, and low mechanical strength. The non-stochastic designs also provided customizable geometry and permeability, enhanced heat transfer, predictable fluid and heat transfer characteristics, and higher mechanical strength, making them ideal for high-performance transpiration cooling in gas turbines. Notably, the mathematical equation-based designs, such as TPMS, exhibited better thermal conductivity, heat and mass transfer, and mechanical strength than the CAD-based designs [84]. In conclusion, the AM-fabricated non-stochastic structures, particularly TPMS-based designs, have demonstrated strong potential for advancing transpiration cooling in gas turbines, motivating the detailed flow and heat transfer analysis in the next section.

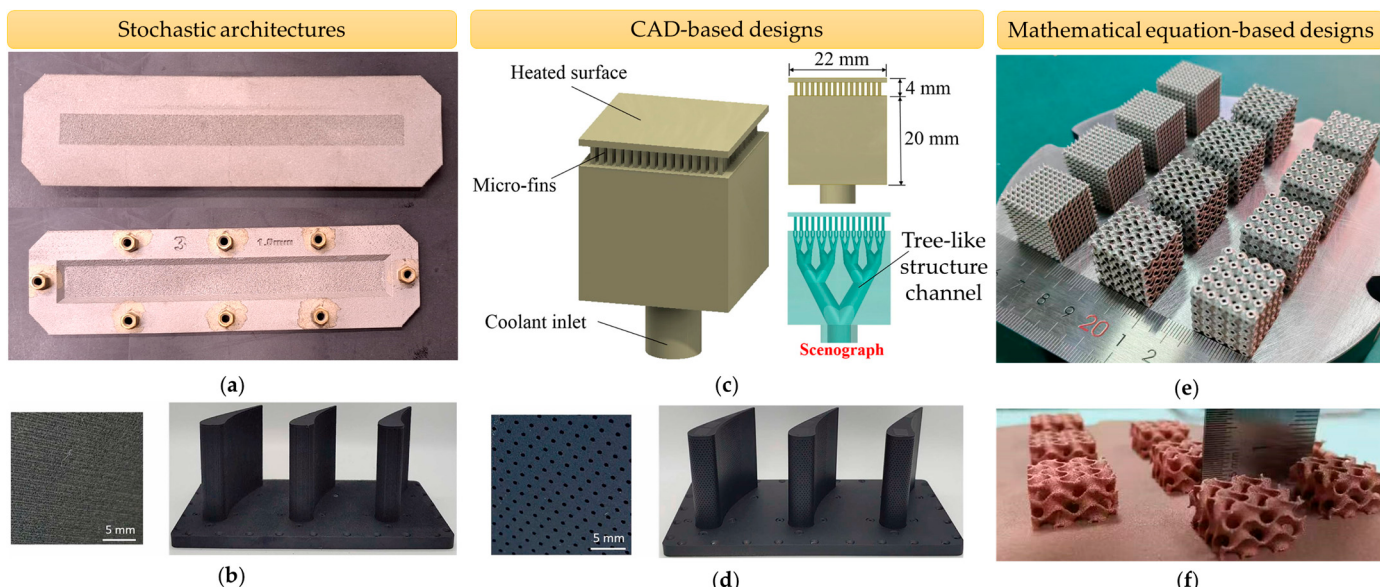


Figure 7. Advanced transpiration cooling structures in recent studies: (a) AM porous Hastelloy-X specimens (Reproduced with permission from [74]. Copyright 2024 Elsevier), (b) AM-fabricated transpiration-cooled cascade blade (Reproduced with permission from [30]. Copyright 2022 Elsevier), (c) Tree-like structure designs (Reproduced with permission from [83]. Copyright 2019 Elsevier), (d) AM-fabricated effusion-cooled cascade blade (Reproduced with permission from [30]. Copyright 2022 Elsevier), (e) Different TPMSs, and (f) Gyroid structures.

4. Flow and Heat Transfer Analysis

4.1. Heat Transfer Mechanism

The general gas-phase transpiration cooling mechanism includes forced convection within the structural matrix and a continuously developing cooling film on the hot gas side of the porous surface that protects the hot gas from attaching to the surface [85], as schematically demonstrated in Figure 8. In gas turbine applications, transpiration cooling also employs this dual-mode heat transfer mechanism to achieve enhanced thermal protection. The internal cooling process involves forced convection through the porous structures or micro holes, where coolant extracts thermal energy from the blade or combustor walls. Then, the coolant forms a film-cooling layer that interacts with the mainstream flow through convective heat transfer within the turbulent boundary layer, mass transfer-driven dilution

of combustion products, and aerodynamic displacement of the stagnation line [37,86]. This combined mechanism enhances cooling effectiveness compared to discrete film cooling, primarily by eliminating jet lift-off effects.

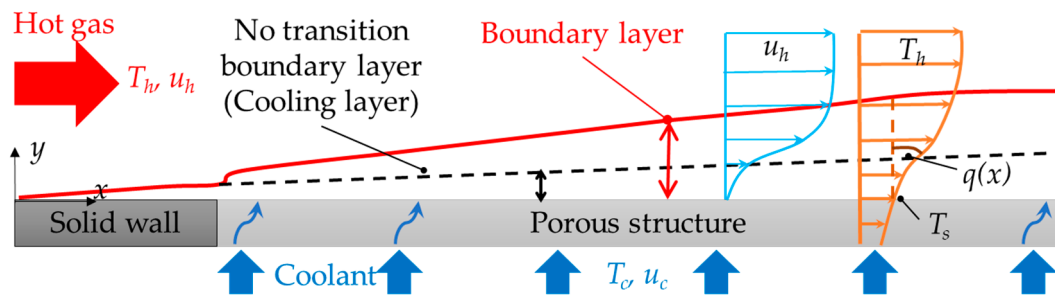


Figure 8. Schematic diagram of heat transfer mechanism of gas-phase transpiration cooling.

The particle image velocimetry (PIV) image and instantaneous velocity distribution [49] in Figure 9 show that the boundary layer remains thin in the initial cooling development region of a relatively small-diameter perforated plate. As coolant air accumulates downstream, progressive boundary layer growth is observed through the transition zone until reaching the developed cooling region. Within the developed cooling area along the wall, the boundary layer thickness stabilizes, maintaining near-constant values across the entire stabilized zone. Additionally, the boundary layer growth rate strongly depends on the cooling supplied rate, increasing linearly with coolant mass flux. Overall, this relationship closely resembles that in the sintered porous-based transpiration cooling structure [49]. Therefore, the diagram in Figure 8 could also be used to explain the flow and heat transfer phenomena of non-stochastic architectures fabricated through AM technology.

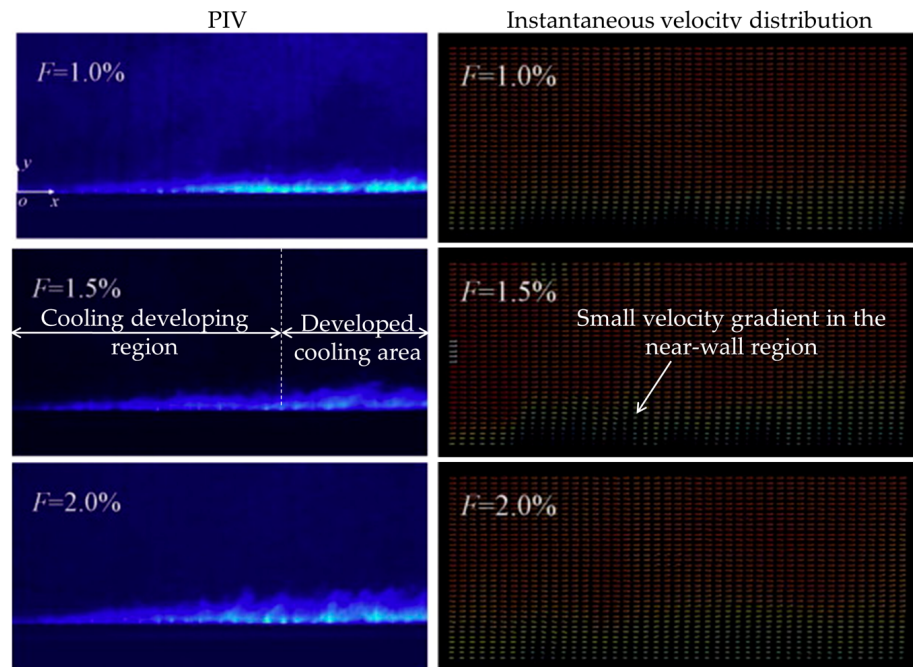


Figure 9. PIV and instantaneous velocity distributions in the near wall region of a perforated transpiration cooling plate. Reproduced with permission from [49]. Copyright 2015 Elsevier.

4.2. Related Parameters

Many pore-scale studies of transpiration cooling couple the high Reynolds number flow of the mainstream (Re_h) and the low Reynolds number flow of the coolant inside the porous matrix (Re_c) [82,87,88], defined as follows:

$$Re_h = \frac{\rho_h u_h d_h}{\mu}, d_h = 4A_h/C_h \quad (1)$$

$$Re_c = \frac{\rho_c u_D d_c}{\mu}, d_c = 4\varphi/S_v \quad (2)$$

where u_h is the mainstream flow velocity (m/s). ρ_c and ρ_h are the densities of coolant and mainstream (kg/m³). d_h , A_h , C_h are the hydraulic diameter (m), cross-sectional area (m²), and the circumference of the hot flow channel (m). μ signifies the dynamic viscosity of fluid (kg/(m·s)). u_D is the Darcy velocity (m/s). d_c is the hydraulic diameter of the coolant supply channel, and S_v is the specific surface area (1/m).

In transpiration cooling experiments, the mass flow ratio of coolant to mainstream (MFR), injection ratio (F), and blowing ratio (BR) are the key parameters for determining the coolant flow rate. The MFR is used in system-level cooling efficiency, such as nose cone and turbine blade cooling, to evaluate coolant supply requirements for a given cooling strategy. The MFR is calculated as follows:

$$MFR = \frac{\dot{m}_c}{\dot{m}_h} \quad (3)$$

where \dot{m}_c and \dot{m}_h are the mass flow rate of the coolant and mainstream (kg/s).

The coolant injection ratio (F) is used when focusing on coolant distribution per unit area, defined as follows:

$$F = \frac{\rho_c u_c}{\rho_h u_h} \quad (4)$$

$$u_c = \frac{\dot{m}_c}{\rho_c A_{eff}} \quad (5)$$

where u_c is the equivalent average cross-section coolant velocity (m/s). A_{eff} is the coolant-covered area on the hot-side surface (m²).

In film or effusion cooling, the blowing ratio (BR) is the primary parameter for evaluating the coolant flow rate, focusing on momentum interaction at the injection point. Unlike the F , the BR is based on the coolant velocity defined per hole/pore rather than the total mass flow rate. The blowing ratio (BR) is expressed as

$$BR = \frac{\rho_c v_c}{\rho_h u_h} \quad (6)$$

where v_c is the average velocity of coolant flow in the film hole (m/s).

The v_c can be derived from the coolant flow rate and the equivalent pore diameter (d_{pore}) of the porous structure in transpiration cooling studies. Due to the significant momentum loss caused by friction within the porous medium, most studies avoid comparing micro-cooling performance using the BR . Instead, cooling effectiveness in various transpiration cooling studies is evaluated based on the injection ratio (F) or the volumetric flow rate (\dot{V}) of the coolant.

The convective heat transfer coefficient (h) and Nusselt number (Nu) are also important parameters to make data comparable for different transpiration cooling designs. The h

(W/m²K) and Nu on the hot-side surface of transpiration cooling structures are defined as follows:

$$h = \frac{Q_{tot}}{A_w(T_h - T_s)} \quad (7)$$

$$Nu = \frac{hL_c}{k_f} \quad (8)$$

where Q_{tot} is the total heat transfer (W). A_w is the wetted area (m²). T_h is the mainstream and coolant temperatures (K). T_s is the surface temperature (K). L_c is the characteristic length of the transpiration cooling designs (m). k_f is the thermal conductivity of fluid (W/m·K).

Generally, for external cooling, the heat transfer analysis quantifies cooling performance through local cooling effectiveness, calculated as

$$\eta = \frac{T_h - T_s}{T_h - T_c} \quad (9)$$

where T_c is the coolant temperature (K).

Film cooling effectiveness (η_a) is typically used in adiabatic wall studies to evaluate localized cooling performance at specific coolant injection points. In contrast, overall cooling effectiveness (η_o) is applied in conjugate heat transfer analyses, assessing the total temperature reduction in the component by accounting for external film cooling and internal cooling mechanisms, that is, the coolant flow through holes or pores.

The Biot number (Bi) is also used to analyze the thermal behavior of porous structures and the efficiency of heat transfer between the solid matrix and the coolant in transpiration cooling [89]. It can be expressed as

$$Bi = \frac{ht}{k_s} \quad (10)$$

where t is the thickness of transpiration cooling structures (m). k_s is the thermal conductivity of the solid domain (W/(m·K)). In the case of porous-media structure, k_{eff} , which is effective thermal conductivity (W/(m·K)), is used instead of k_s .

The flow resistance of different transpiration cooling designs is usually evaluated using the total pressure loss coefficient (ζ_{Pt}) [82,90], defined as

$$\zeta_{Pt} = \frac{p_{t,in} - p_{t,out}}{p_{t,in}} \quad (11)$$

where $p_{t,in}$ and $p_{t,out}$ are the total pressure of the coolant inlet and outlet (Pa), respectively.

The skin-friction coefficient (CF) of the transpiration cooling is employed to reveal the shear stress (τ_w) on the solid surface due to the viscous effects and show the attachment of the coolant film [91]. The CF is expressed as follows:

$$CF = \frac{\tau_w}{0.5\rho_h u_h^2} \quad (12)$$

Another parameter used to quantify the efficiency of the flow contraction through transpiration cooling structures and viscous loss due to the tortuosity of the transpiration topology is the discharge coefficient (CD). The CD is defined as the ratio of the actual mass flow rate to the theoretical mass flow rate [75,79], which can be simplified as follows:

$$CD = \frac{\dot{m}_c}{A_{pore} \sqrt{2\rho_c(p_{t,in} - p_{t,out})}} \quad (13)$$

where A_{pore} is the total cross-sectional area of transpiration cooling topology (m²).

Due to material shrinkage, printing resolution, and post-processing, the AM structures often exhibit dimensional variations from their original designs. To assess these manufacturing tolerances, both the designed porosity (φ_{des}) and actual porosity (φ_{act}) of test specimens are quantified using

$$\varphi_{des} = \left(1 - \frac{V_{des}}{V_{sol}}\right) \times 100\% \quad (14)$$

$$\varphi_{act} = \left(1 - \frac{M_{des}}{M_{sol}}\right) \times 100\% \quad (15)$$

where V_{des} represents the designed volume of a geometry from a CAD model (m^3). V_{sol} is the volume of a solid domain with identical dimensions (m^3). M_{des} signifies the measured weight of a test specimen, while M_{sol} is the measured weight of the solid plate (kg).

Additionally, to analyze the influence of transpiration cooling design on heat transfer, the internal surface area ratio (R_{int}) and outlet area ratio (R_{out}) are usually presented [76,92], which can be calculated as

$$R_{int} = A_{int} / A_{eff} \quad (16)$$

$$R_{out} = \frac{A_{out}}{A_{eff}} \times 100\% \quad (17)$$

where A_{int} and A_{out} are the internal surfaces of the solid–fluid interface inside the specimens and the outlet area of the coolant at the outer surface (m^2), respectively. These area values are typically derived from CAD models.

4.3. Experimental Research

4.3.1. Experimental Setup and Measurement Method

Experiments on AM-based transpiration cooling structures are essential to address various aspects, such as the effect of geometrical designs and the influence of studied conditions, which analytical models often inadequately represent [93,94]. The experimental studies validate theoretical assumptions, reveal the interactions of porosity (φ) or topology on thermo-fluidic behavior, and quantify flow distribution in complex AM geometries. The general experimental setup for analyzing the flow and heat transfer of transpiration cooling is schematically depicted in Figure 10a.

The airflow generated by the blower or compressor passes through the inlet diffuser and enters the heater uniformly, where it is heated to the target temperature. The heated air then flows through flow stabilizers, such as honeycombs or mesh screens, to ensure a uniform mainstream flow within the test section. Maintaining consistent temperature and velocity of the mainstream inside the test section is critical. Additionally, the turbulent intensity of the airflow must be measured. For the coolant system, the coolant is supplied by the blower or compressor, and its flow rate can be adjusted using a flowmeter to vary the MRF , BR , or F . In flow visualization studies, techniques such as smoke-laser sheet imaging [30,73,95] or PIV [49] may be employed.

Pressure-sensitive paint (PSP) and infrared thermography (IR) methods have been widely used to acquire the cooling effectiveness of the transpiration cooling wall, as demonstrated in examples in Figure 10b,c. Meanwhile, the use of transient liquid crystal thermography (TLC) was quite limited. The PSP method measures surface pressure distributions indirectly by detecting oxygen quenching of luminescent molecules, which can then be correlated to temperature in certain applications. It provides high spatial resolution and is particularly useful for aerodynamic studies, but it requires optical access and careful calibration to separate pressure and thermal effects. In contrast, IR thermography directly captures surface temperature distributions by detecting thermal radiation emitted by the

material. IR is non-invasive, works in real-time, and is well-suited for thermal analysis, but its accuracy can be affected by surface emissivity variations and environmental reflections. While PSP excels in detailed pressure mapping with temperature derivations, IR is more straightforward for pure thermal visualization, making them complementary tools depending on the experimental focus.

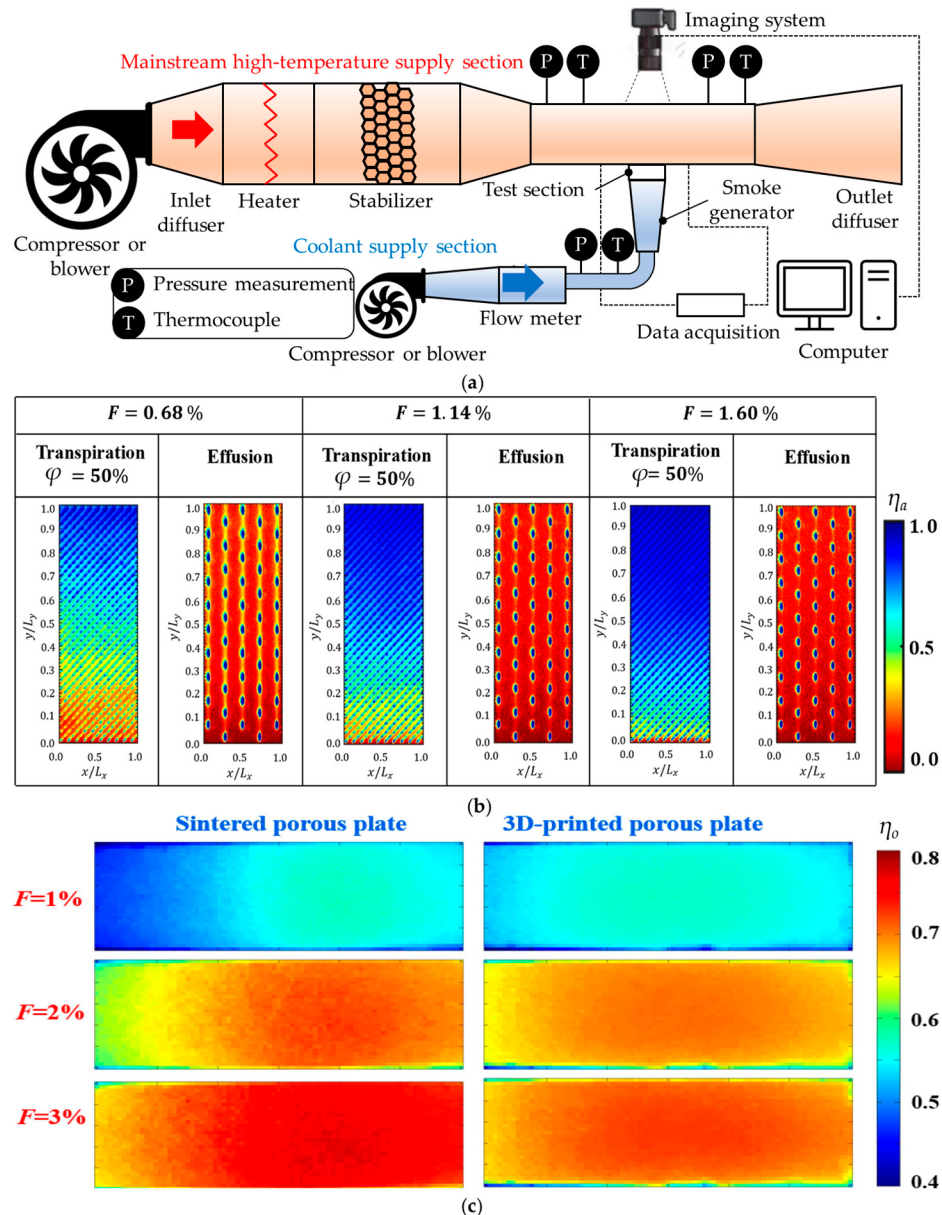


Figure 10. General experimental setup for investigation on flow and heat transfer of transpiration cooling: (a) Schematic diagram; (b) Illustration of η_a contours (Reproduced with permission from [92]. Copyright 2024 Elsevier) and (c) η_o distributions (Reproduced with permission from [51]. Copyright 2018 Elsevier).

Recent experimental studies on flow and heat transfer of AM transpiration cooling, suited for gas turbine applications, have been conducted, as shown in Table 2. Different measurement techniques used to acquire η , heat transfer coefficient (h), velocity (u), and discharge coefficient (CD) under various conditions are summarized. This study evaluated transpiration cooling performance across various designs, with area-averaged effectiveness (η_o and η_a) ranging from 0.05 to 0.95. Optimal configurations included sintered models with an area-averaged η_o of 0.74, staggered arrangements on an SS turbine blade with an

area-averaged η_a of 0.95, and bio-inspired structures with an area-averaged η_o of 0.35–0.57. Graded porosity reduced peak temperatures by 20%, while inserting a lattice decreased area-averaged η_o by 12%. The results demonstrate that cooling efficiency was highly dependent on geometry and φ distribution.

Table 2. Overview of experimental studies on flow and heat transfer of AM transpiration cooling.

Ref.	Studied Models	Measurement Techniques (Evaluated Metric)	Studied Conditions	Significant Results
[73]	A C3X single-turbine blade with different cooling methods	IR thermography (η_o)	$T_h = 100^\circ\text{C}$; $T_c = 20^\circ\text{C}$; Mainstream Reynolds number (Re_h) = 100,000 ($u_h = 20 \text{ m/s}$); Volumetric flow rate of coolant (\dot{V}_c) = 100–400 LPM	The maximum area-averaged η_o of the transpiration-cooled single turbine blade was 0.58.
[95]		Smoke-laser with a high-speed camera (u)	$T_h = T_c = 6.5^\circ\text{C}$; $Re_h = 10,000$ ($u_h = 2 \text{ m/s}$); $\dot{V}_c = 0$ –200 LPM; $BR = 4.2$ –21.2	The coolant film on the transpiration-cooled blade was more stable.
[30]	A C3X cascade-turbine blade with different cooling strategies	IR thermography (η_o) Smoke-laser with a high-speed camera (u) TLC	$T_h = 100^\circ\text{C}$; $T_c = 20^\circ\text{C}$; $Re_h = 50,000$ –100,000 ($u_h = 10$ –20 m/s); $\dot{V}_c = 50$ –300 LPM	The maximum area-averaged η_o of the transpiration-cooled cascade turbine blade was 0.7.
[74]	Porous-media transpiration-cooled plates	(h , η_a) IR flow visualization (u)	$T_h = 70^\circ\text{C}$; $T_c = \text{Ambient temperature}$ (T_{Amb}); $Re_h = 25,000$ ($u_h = 3.4 \text{ m/s}$); $BR \approx 0.4$ –2.0	The highest area-averaged η_a of the transpiration-cooled plates was less than 0.4.
[75]	Porous-media transpiration-cooled specimens	Static pressure taps (CD)	The ratio of plenum stagnation and atmospheric pressures (PR) = 1.02–1.7.	The CD of the 90° laser direction was 0.02–0.07, lower than that of the 67° model.
[64]	Uniform and graded IWP TPMS plates	IR thermography (T)	$T_h = 420$ –480 K; Mach number of mainstream (Ma_h) = 2.8; $F = 0.1$ –0.6%.	The graded IWP reduced the maximum local temperature by around 20% compared to a uniform one.
[79]	Transpiration cooling combined with lattice structures on a leading edge	Static pressure taps (CD)	$PR = 1$ –1.3.	The highest CD was 0.17 in the impingement sleeve.
[96]		PSP (η_a)	$T_c = T_{amb}$; $Re_h = 825,313$; $BR = 0.03$ –0.15.	The area-averaged η_a was 0.11–0.34, and the maximum pressure loss was about 4.4 kPa.
[97]	Perforated transpiration-cooled turbine blade	PSP (η_a)	$T_h = T_{Amb}$; $Re_h = 1.2 \times 10^6$ ($Ma_h = 0.3$); $m_c = 5$ –20 g/s ($BR \approx 0.1$ –0.5).	The staggered arrangement on the SS turbine blade showed the highest area-averaged η_a of 0.95.
[51]	Partitional walls in transpiration-cooled plates	IR thermography (η_o)	$T_h = 340 \text{ K}$; $T_c = 296 \text{ K}$; $u_h = 11 \text{ m/s}$; $F = 1$ –3%	The maximum area-averaged η_o of the sintered and AM models was 0.74 and 0.71.
[98]		PSP (η_a)	$Re_h = 395,000$ ($u_h = 21.6 \text{ m/s}$); $BR = 0.1$ –0.7.	The highest area-averaged η_a values of the 0% and 60% blockage models were about 0.68 and 0.4.
[76]	Different transpiration topology designs		$T_h = 45$ –60 °C; $T_c = 21^\circ\text{C}$; $Re_h = 98,000$ ($u_h = 11 \text{ m/s}$); $BR = 1$ –3; $F = 1.2$ –3.6%.	The blood vessel-shaped designs showed η_o of 0.35–0.57.
[77]	Different perforated transpiration designs	IR thermography (η_o)		The optimal design was the 3d-pitch ($d = 0.3 \text{ mm}$) with η_o of 0.48 and a relative UTS of 0.74.
[78]	Integrated lattice transpiration cooling structures		$T_h = 50$ –60 °C; $T_c = 21^\circ\text{C}$; $Re_h = 98,000$ ($u_h = 11 \text{ m/s}$); $F = 1.0$ –2.5%.	The area-averaged η_o was reduced by 12% when inserting a lattice in the transpiration-cooled plate. The highest area-averaged η_o was 0.67 in the pure transpiration cooling model.
[99]	Different perforated transpiration designs	IR thermography (η_a)	$T_h = 50^\circ\text{C}$; $T_c = 21^\circ\text{C}$; $BR = 0.125$ –0.5	The spanwise-averaged η_a increased from 0.44 to 0.73 in the $2.5d$ -pitch ($d = 0.5 \text{ mm}$) at $BR = 0.5$, higher than various multirow film hole studies.
[100]	Wire mesh porous transpiration-cooled plate	IR thermography (η_a)	$T_h = 295 \text{ K}$; $T_c = 21^\circ\text{C}$; $u_h = 18.8 \text{ m/s}$; $F = 0.4$ –5.2%.	The area-averaged η_a values were within 0.05–0.36.
[101]	Different porosities and injection ratios of the Gyroid TPMS model	IR thermography (η_a)	$T_c = 80^\circ\text{C}$; $Ma_h \approx 0.27$ ($u_h = 87.5 \text{ m/s}$); $\rho_h/\rho_c = 0.83$; $F = 1.4$ –3.1%.	The area-averaged η_a values were around 0.3–0.5.
[92]	Different porosities of Diamond TPMS plates			The model with the φ of 30%, 40%, and 50% showed the highest area-averaged η_a by 0.49, 0.69, and 0.75.
[81]	Different TPMS transpiration cooling designs	PSP (η_a)	$T_h = 50$ –60 °C; $Re_h = 256,000$ ($u_h = 33 \text{ m/s}$); $F = 0.68$ –1.60%.	The Diamond, Gyroid, and Koch models demonstrated the maximum area-averaged η_a by 0.76, 0.71, and 0.79.
[102]	Different unit cell sizes of Diamond TPMS plates			The model with the unit cell size (L) of 1.9, 2.5, and 3.1 mm provided the highest area-averaged η_a by 0.75, 0.71, and 0.66.

4.3.2. Experimental Studies on AM-Fabricated Random-Pore Porous Structures

The Korea Advanced Institute of Science and Technology pioneered innovative experimental research on state-of-the-art transpiration-cooled C3X turbine blades, showing remarkable ingenuity in advancing thermal protection for cutting-edge gas turbine cooling.

Kim et al. [73] compared internal, effusion, and 3D printed-porous transpiration cooling. The test section featured CaF₂ windows with 95% transmittance at 3–5 μm to minimize thermal interference, enabling accurate IR thermometry. The studied models included a 0.5 mm effusion-hole model fabricated by electric discharge machining and a 40 μm porous-based transpiration cooling model structure, additively manufactured within $\varphi = 53\%$. The results showed that transpiration cooling demonstrated superior performance, achieving 34% and 25% higher η_o than effusion and internal cooling. The cooling effectiveness of the transpiration cooling model was more uniform, especially on the pressure side (PS).

Kim et al. [95] also used smoke-laser visualization with two diode-pumped solid-state lasers and olive oil seeding to visualize coolant flow release from the blade; then, the flow characteristics were captured by a high-speed CCD camera. It was revealed that transpiration cooling provided uniform coverage and low-momentum discharge, which prevented recirculation flow, while effusion cooling showed a large layer thickness, as shown in Figure 11a. Despite comparable coolant-to-mainstream pressure ratios, transpiration cooling required less coolant for better performance. A subsequent study [30] was conducted on a C3X cascade-turbine blade compared with different cooling methods, namely internal cooling only, effusion cooling, and transpiration cooling. They observed that in cascade blades, adjacent blades redirected and accelerated the flow along the blade chord, as shown in Figure 11b. It was obvious that the transpiration cooling showed more uniform and higher cooling effectiveness, as seen in Figure 11c. Moreover, compared to a single blade, the coolant outflow formed a thinner boundary layer in effusion and transpiration cooling. This shifted the suction-side vortex rearward, reducing mainstream/coolant mixing and stabilizing the coolant within the boundary layer. Due to these flow interactions, the cascade arrangement enhanced cooling effectiveness, as shown in Figure 11d.

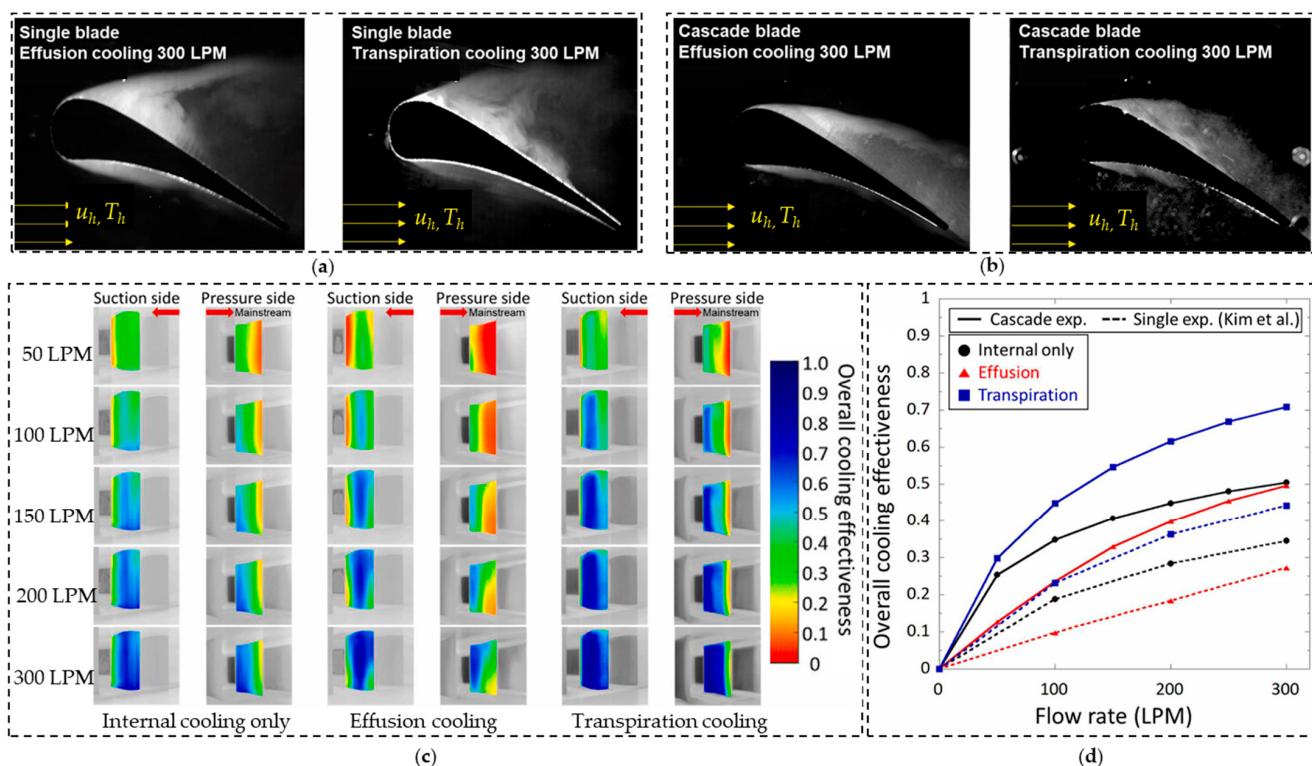


Figure 11. Transpiration-air cooled turbine blade: (a) visualization of coolant flow at $u_h = 20$ m/s and coolant volume flow rate of 300 LPM for the single blade; (b) for the cascade blade; (c) η_o distributions on the cascade blade with different cooling; and (d) comparisons of area-averaged cooling effectiveness between cascade and single-turbine blades from Kim et al. [73]. Reproduced with permission from [30]. Copyright 2022 Elsevier.

Researchers from Siemens Energy AB, Finspong, Sweden [74], evaluated the distributions of h and η_a of a porous Hastelloy-X transpiration-cooled plate against conventional cylindrical film holes using TLC and IR-based flow visualization with water and CO₂. Their results demonstrated that transpiration cooling enhanced lateral-averaged h and η_a compared to the cylindrical holes, owing to superior spanwise coolant coverage and reduced lift-off effects, except at a low $BR = 0.46$. The thickness (t) of the AM porous plate had a minor influence on the local and area-averaged η_a but provided more uniformity, as shown in Figure 12a. They reported that the highest area-averaged η_a was obtained at a $BR = 0.8$, and it sharply declined at the highest $BR = 2.0$ because the excessive coolant supply caused significant jet lift-off and impaired near-wall reattachment, as demonstrated in Figure 12b. To mitigate this, the research team proposed optimizing the build direction of the AM model to achieve a more favorable coolant ejection angle, thereby preserving cooling performance while minimizing flow disturbance from high discharging coolant.

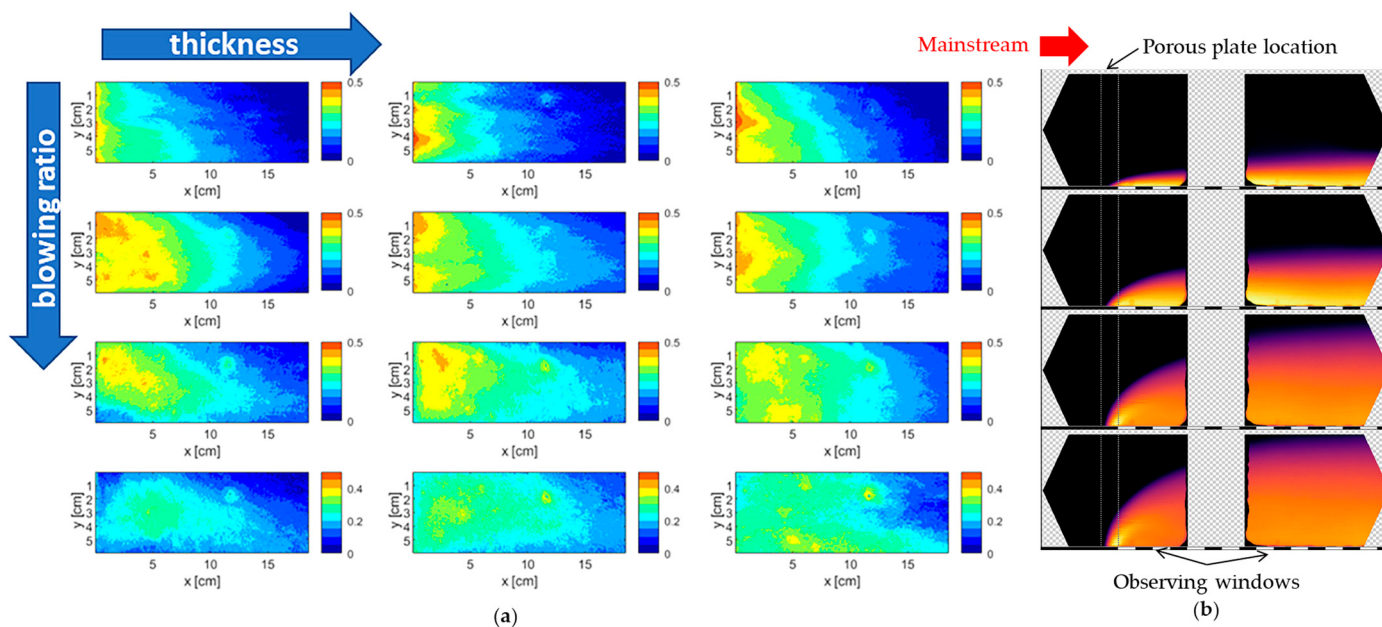


Figure 12. A porous Hastelloy-X transpiration-cooled plate: (a) contours of η_a at $BR = 0.5, 0.8, 1.5$, and 2.0 and $t = 0.5, 1.0$, and 2.0 mm and (b) IR images of concentration of ejected air at $BR = 0.5, 0.8, 1.5$, and 2.0 . Reproduced with permission from [74]. Copyright 2024 Elsevier.

Fantozzi et al. [75] studied the influence of the structural parameters, including laser power, laser speed, and hatch distance of 3D-printed porous materials, on fluid flow, focusing on pore radius distribution and CD . They demonstrated that the CD increased with the pressure ratio and hatch distance but decreased nonlinearly with the thickness-to-diameter ratio. The specimens printed with a laser rotate 90° between layers, providing lower CD values than the model fabricated by a 67° rotation due to the variation in the φ . These studies demonstrated that transpiration cooling outperformed conventional methods in thermal protection, uniformity, and efficiency, with the AM method enabling optimized porous structures for enhanced gas turbine blade performance.

4.3.3. Experimental Investigations on AM-Fabricated Non-Stochastic Structures

Recent advancements in transpiration cooling for gas turbine blades have shown the superior performance of AM-fabricated deterministic structures, such as TPMS and biomimetic designs, over traditional random-pore media. Cheng et al. [64] used deionized water as a coolant for the IWP(A) TPMS-based transpiration cooling with uniform ($\varphi = 35\%$) and graded porosity ($\varphi = 25\text{--}45\%$) to enhance cooling performance. The experi-

ments using IR thermography were conducted to observe the phase change region on the transpiration-cooled plate. Even though phase-change transpiration cooling offers high heat absorption, its complexity and instability, caused by unpredictable two-phase flow dynamics and excessive coolant use, make it impractical for gas turbine applications [103]. In contrast, single-phase transpiration cooling provides more reliable and controllable cooling performance, making it the preferred choice for gas turbines where stability and uniformity are critical.

Experiments on AM transpiration-cooled turbine blades have revealed improved film uniformity and cooling effectiveness. Ealy [79] used multiple static pressures for flow testing of the 0.5 mm perforated transpiration-cooled leading edge (LE) and revealed nearly identical discharge behavior across both internal and external cavities. This flow improved the film uniformity compared to discrete holes, even though the design yielded lower CD due to area calculation discrepancies. In a subsequent study, Caldero et al. [96] studied the η_a using the PSP method. They found that the effectiveness and pressure loss of the porous cavities in the LE increased at higher BR . The discharged coolant was uniform downstream of the porous region, and mixing became more evident with the higher BR .

Similarly, research by Wambersie et al. [97] showed high η_a across a 0.5 mm perforated transpiration-cooled turbine blade at a low $BR < 0.5$. They fabricated the blade using the Stereolithography (SLA) method and employed the PSP measurement that was used in their previous double-wall cooling research [104]. They found high performance on the suction-side (SS) turbine blade due to curvature and flow acceleration, enabling uniform cooling, as shown in Figure 13a,c. While the pressure side (PS) showed the lowest area-averaged η_a , large areas maintained high film effectiveness, as illustrated in Figure 13b,d. This key achievement could help justify reallocating the coolant supply. Moreover, compared to a turbine blade with impingement/effusion cooling, the transpiration cooling at the SS and PS blades provided higher area-averaged η_a and a more uniform distribution.

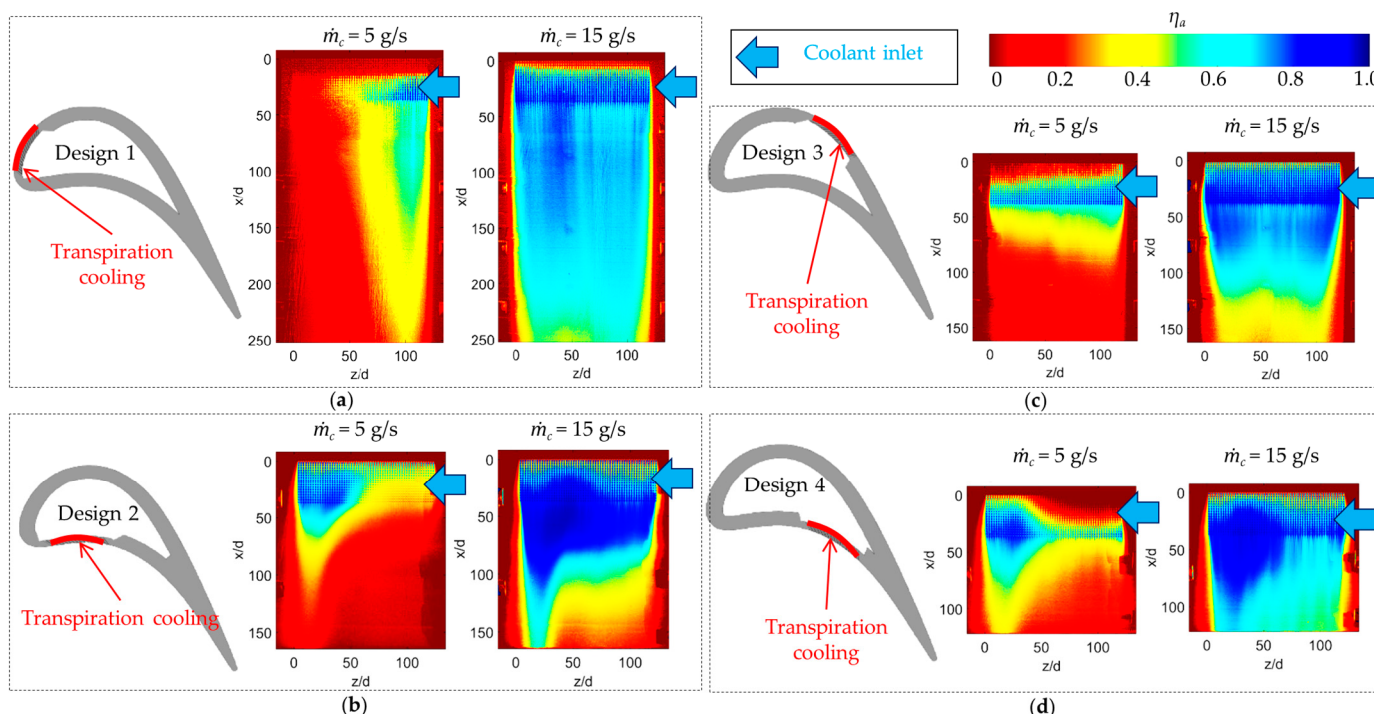


Figure 13. Distribution of η_a on transpiration-cooled blade: (a) SS cooling (Design 1); (b) PS cooling (Design 2); (c) SS cooling (Design 3); and (d) PS cooling (Design 4). This figure is reproduced from [97] under a Creative Commons Attribution (CC BY) license.

The perforated transpiration-cooled plates have been intensively studied by the research team from the National Energy Technology Laboratory, with the cooperation of the University of Pittsburgh and West Virginia University. Min et al. [77] studied various hole designs, including inline straight holes with a pitch of $1.5 d$, $2 d$, and $3 d$, staggered straight holes with a pitch of $2 d$, and 20° inclined holes with a pitch of $2 d$. The hole diameter (d) also varied from 0.3 to 0.5 mm. In conclusion, as shown in Figure 14, the smaller holes ($d = 0.3$ mm) and spacing (pitch of $1.5 d$) showed the highest and most uniform η_o but caused low mechanical strength. Chyu et al. [78] reported that integrating lattices with transpiration cooling causes a slightly lower area-averaged η_o due to partial obstruction of cooling holes by the footprint. However, the lattices mitigated η_o losses from pore blockages and offered a better alternative to pin fins for structural support due to their high surface-to-footprint ratio, addressing the inherent weakness of transpiration-only designs.

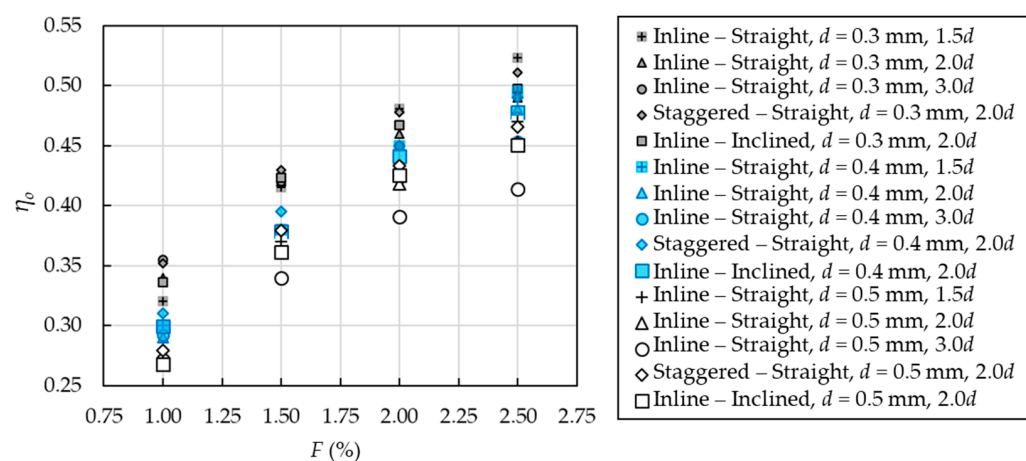


Figure 14. Area-averaged η_o comparisons at different F . Data collected from [77].

Heat transfer analysis on innovative hole designs of transpiration-cooled plates has been attempted by many research institutes. Huang et al. [51] compared the effects of partition walls on 0.3 mm perforated transpiration-cooled plates using IR thermography. They found that at a low $F = 1\%$, the printed models with/without partition walls provided a similar area-averaged η_o value, which was higher than the sintered porous model ($d_{pore} = 90 \mu\text{m}$, $\varphi = 32\%$, pore size = $33.8 \mu\text{m}$). However, the sintered porous model was sensitive to the increase in coolant supply, generating a higher area-averaged η_o than the printed models when $F > 2\%$ due to increasing detached coolant on the surface of the printed model. In line with the earlier configuration, Min et al. [76] used IR thermography to investigate five topology designs for AM transpiration-cooled plates, including two perforated plates with varying hole pitches, a sphere-packing design, a wire matrix resembling woven mesh, and a biomimetic blood vessel structure. All studied F demonstrated a superior area-averaged η_o of all transpiration designs over shaped-hole film cooling by 10–40%. They found that the topology of the 3D-printed transpiration-cooled plate significantly influenced the η_o .

Experiments on non-metal transpiration cooling structures have been performed to assess the adiabatic film cooling effectiveness (η_a). Min et al. [99] developed a physical vapor deposition (PVD) micro-lithography technique to fabricate a surface heater for testing transpiration cooling. The IR thermography revealed that smaller coolant hole spacing and diameters improved $\eta_a > 0.46$, outperforming conventional film cooling. Aly et al. [98], employing the PSP method to study the influence of the blockage ratio on the η_a , revealed that increasing the blockage ratio reduced the area-averaged η_a , particularly at lower BR , due to a smaller coolant supply. Higher BR and blockage ratio caused

non-uniform η_a distributions within the row. Moreover, larger blockage ratios reduced lateral effectiveness, while higher BR compensated for insufficient coolant supply. In short, although the innovative partition wall designs reduced thermal efficiency, potential improvements included shaped holes, extended surfaces, vortex generators, and AM rough surfaces.

A more complex structure has been fabricated to address non-uniformity, increase cooling effectiveness, and further strengthen the structure. Fier and Bogard [100] fabricated a wire-mesh transpiration-cooled plate using a Prusa i3 3D printer based on fused deposition modeling (FDM). The proposed design demonstrated superior performance to traditional 7-7-7-shaped film-cooling holes, achieving up to 30% higher η_a at equal coolant flow rates. Brimacombe et al. [101] claimed to be the first use of the Gyroid TPMS-based transpiration cooling, 3D-printed via the SLA method at a 25 μm resolution with a 2 mm unit cell size. The IR thermography was used to measure the temperature distribution far downstream from the Gyroid-cooled plate, as shown in Figure 15a. The results showed that increasing BR and F increased the η_a , but the η_a was more sensitive to φ at a constant BR than at a fixed F , as seen in Figure 15b. The area-averaged η_a was higher than that of effusion cooling [105] but less than that of the AM wire-mesh transpiration-cooled plate with $\varphi = 33\%$ [100], which could be attributed to the distance of the measurement area.

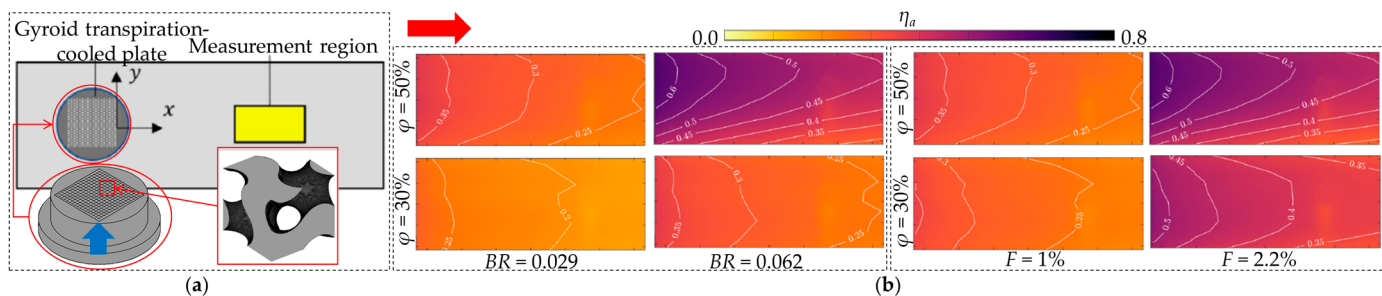


Figure 15. Gyroid TPMS-based transpiration-cooled plate: (a) Downstream heat transfer measurement and (b) the distribution of η_a at different BR , F , and φ . This figure is reproduced from [101] under a Creative Commons Attribution (CC BY) license.

The research team from the Aerospace Research Center, National Research Council of Canada has intensively conducted the heat transfer analysis of the TPMS-based transpiration cooling. Broumand et al. [92] found that the Diamond TPMS-based transpiration-cooled plate with $\varphi = 50\%$ outperformed conventional effusion cooling by up to five times in the area-averaged η_a using the PSP method, where the calibration and uncertainty were well-described in the report. They also revealed that the TPMS designs provided superior film coverage, reduced coolant usage, and mitigated film lift-off at high BR [106]. Using the same measurement method, Son et al. [81] found that the orientation and tortuosity of Diamond, Koch, and Gyroid TPMS topologies altered the distribution of η_a on the plate. Later, Son et al. [102] studied the variations in the unit cell size (L) of the Diamond model while maintaining φ . They found that reducing the L improved η_a . However, excessively small sizes could risk pore blockage from 3D printing or contamination, requiring optimal sizing in practical use.

4.4. Numerical Simulations

Computational modeling of transpiration cooling requires balancing accuracy and efficiency, especially when simulating phase-change effects or resolving complex porous structures. The porous-media two-phase flow model simplifies the simulation of phase-change transpiration cooling, where liquid coolant boils inside the porous structure, forming a gas–liquid mixture [107]. The phase transition absorbs significant latent heat, enhancing

cooling efficiency. However, the inherent instability of boiling and non-uniform two-phase flow makes this method more complex than single-phase transpiration cooling [64]. Alternatively, Zhang et al. [80] employed the Lattice Boltzmann Method (LBM) to simulate flow through printed TPMS structures, comparing CAD and computed tomography (CT) scan geometries. They demonstrated the efficiency of the LBM in handling the complex TPMS boundaries through simple voxelized meshes, avoiding the costly unstructured meshes in conventional Navier–Stokes (NS) solvers. However, the LBM struggles with high Reynolds flows, which is the inertial regime in transpiration cooling, whereas the NS solvers with Reynolds-averaged Navier–Stokes (RANS) or large eddy simulation (LES) are more mature. Additionally, the LBM faced scalability limitations for graded or optimized complex topologies, such as the TPMS structure, requiring fine voxel resolutions. Modern NS solvers, in contrast, leverage advanced turbulence modeling to capture multiscale phenomena computationally efficiently for large-scale academic/industrial flow/heat transfer and optimization analyses.

In general, the governing equations for single-phase transpiration cooling can also be divided based on structures: deterministic and stochastic architectures. Table 3 compares the governing equations based on steady-state and non-radiation assumptions. In Table 3, ρ is the density of the fluid (kg/m^3). \mathbf{u} is the velocity vector (m/s). S_m is a mass source term representing fluid injection from the wall during the cooling of porous transpiration (N/m^3). p is the pressure field, signifying the static pressure in the domain (N/m^2). \mathbf{F} implies an external force, such as gravity (N/m^3). c_p is the heat capacity of the fluid ($\text{J}/(\text{kg}\cdot\text{K})$). T_{flu} and T_{sol} are the temperatures of the fluid and solid (K). S_T is the term for the energy source added/removed with the coolant (W/m^3). K and C_F are the permeability (m^2) and inertial resistance coefficient ($1/\text{m}$), where the empirical formula provided by Ergun and Orning [108] was mostly used.

Table 3. Governing equations of single-phase transpiration cooling in recent numerical studies.

Equation	Non-Stochastic Transpiration	Random-Pore Porous-Media Model
Mass conservation	$\nabla \cdot (\rho \mathbf{u}) = 0$	$\nabla \cdot (\rho \mathbf{u}) = S_m$
Momentum	$\rho(\mathbf{u} \cdot \nabla \mathbf{u}) = -\nabla p + \mu \nabla^2 \mathbf{u} + \mathbf{F}$	$\frac{\rho}{\varphi^2}(\mathbf{u} \cdot \nabla) \mathbf{u} = -\nabla p + \mu \nabla^2 \mathbf{u} - \left(\frac{\mu}{K} + \frac{\rho C_F}{\sqrt{K}} \mathbf{u} \right) \mathbf{u}$ $K = \frac{d_{pore}^2 \varphi^3}{150(1-\varphi^2)}; C_F = \frac{1.75}{\sqrt{150}\varphi^{3/2}}$
Energy (Fluid)	$\rho c_p (\mathbf{u} \cdot \nabla T) = \nabla \cdot (k_f \nabla T)$	$\rho c_p (\mathbf{u} \cdot \nabla T) = \nabla \cdot (k_{eff} \nabla T) + S_T$ $k_{eff} = \varphi k_f + (1-\varphi)k_s$
Energy (Solid)	$\nabla \cdot (k_s \nabla T) = 0$ (no internal heat generation)	$\nabla \cdot (k_s \nabla T) = 0$
Fluid–solid interface boundary conditions	$T_{flu} = T_{sol}$ $-k_f \nabla T \cdot \mathbf{n} = -k_s \nabla T \cdot \mathbf{n}$	

For both modes, recent numerical investigations have employed advanced computational fluid dynamics (CFD) tools to analyze various transpiration cooling configurations, utilizing different turbulence models and mesh strategies, as shown in Table 4. Major studies used STAR-CCM+ and ANSYS FLUENT with hexahedral meshes ranging from 2.3 million to 53.4 million cells, depending on the complexity of the model. The $k-\omega$ turbulence model showed the advantage of simulating the viscous sub-layer and boundary layer formation and obtained better predictability in heat transfer analysis compared to SST $k-\omega$ turbulence models in several studies [109].

Table 4. Overview of numerical analysis on flow and cooling effectiveness for AM-fabricated transpiration cooling.

Ref.	Main Study	Tool	Method	Material	Mesh Details
[95]	Flow characteristics on a transpiration-cooled single-turbine blade	STAR-CCM+	$k-\omega$	Porous media with stainless steel in the transpiration model	<ul style="list-style-type: none"> Hexahedral mesh = 15.3×10^6 cells for effusion and = 9.5×10^6 cells for transpiration cooling.
[30]	Flow and temperature distributions on a transpiration-cooled cascade-turbine blade	STAR-CCM+	SST $k-\omega$		<ul style="list-style-type: none"> Hexahedral mesh = 53.4×10^6 cells for effusion and = 2.3×10^6 cells for transpiration cooling.
[25]	Flow and overall cooling effectiveness of a non-uniform porosity transpiration-cooled blade	ANSYS FLUENT	SST $k-\omega$		<ul style="list-style-type: none"> Hexahedral mesh = 3.46×10^6 cells generated by FLUENT Meshing
[96]	Adiabatic cooling effectiveness and pressure loss of transpiration-cooled leading edge	STAR-CCM+	SST $k-\omega$	Adiabatic	<ul style="list-style-type: none"> Polyhedral mesh = 8.44×10^6
[110]	Effects of outlet angle and pattern on transpiration-cooled plates	ANSYS FLUENT	SST $k-\omega$	Inconel 600	<ul style="list-style-type: none"> Structured mesh = 1.07×10^6 cells
[82]	Transpiration-cooled plates with TPMS structures	ANSYS FLUENT	SST $k-\omega$	Stainless steel	<ul style="list-style-type: none"> Polygonal mesh = 5.21×10^6 cells generated by FLUENT Meshing
[51]	Effects of partitional walls on flow and overall cooling effectiveness in transpiration-cooled plates	ANSYS FLUENT	$k-\omega$	Inconel 718	<ul style="list-style-type: none"> Quadrilateral mesh = 2.0×10^6
[111,112]	Pore blockage effects on perforated transpiration-cooled plates	ANSYS CFX	SST $k-\omega$	$k_s = 1 \text{ W}/(\text{m}\cdot\text{K})$	<ul style="list-style-type: none"> Hexahedral mesh = 3.1×10^6 cells
[113]	Pore blockage effects on tree-like transpiration-cooled plates	ANSYS FLUENT	SST $k-\omega$	Inconel 718	<ul style="list-style-type: none"> Polyhedral mesh = 5.66×10^6 cells, generated by FLUENT Meshing
[114]	Pore blockage effects on the oriented porous structure	ANSYS FLUENT	-	Porous media with CMC ($k_s = 2 \text{ W}/(\text{m}\cdot\text{K})$)	<ul style="list-style-type: none"> Porous: $\varphi = 30\%$, $d_{pore} = 0.1 \text{ mm}$, resulting in mesh = 186,500 cells
[89]	Effects of hole diameter, Biot number, and coolant distribution on perforated transpiration-cooled plates	ANSYS FLUENT	SST $k-\omega$	Inconel 718	<ul style="list-style-type: none"> Structured mesh and O-block with local refinement = 1.96×10^6 cells
[115]	Effects of solid thermal conductivity, wall thickness, hole spacing, and TBC on AM transpiration cooling plates with inhomogeneous porosity	ANSYS FLUENT	$k-\omega$	Inconel 718 and ceramic ($k_s = 1, 11$ and $50 \text{ W}/(\text{m}\cdot\text{K})$)	<ul style="list-style-type: none"> Hexahedral mesh = 1.43×10^6 cells generated by ANSYS ICEM
[116]	Transpiration-cooled plates with varied porosity configurations and pressure gradients	ANSYS FLUENT	SST $k-\omega$	Inconel 718 (Temperature-dependent properties)	<ul style="list-style-type: none"> Hexahedral mesh = 16.38×10^6 cells generated by ANSYS ICEM
[117]	Swirl-chamber effusion with different inclination angles and compound angles	ANSYS FLUENT	RSM	$k_s = 0.5 \text{ W}/(\text{m}\cdot\text{K})$	<ul style="list-style-type: none"> Hexahedral mesh = 18.5×10^6 cells

However, the SST $k-\omega$ model was mostly employed to examine transpiration cooling for gas turbines due to its unique ability to accurately resolve near-wall flow physics, adverse pressure gradients, and mixing phenomena. The SST $k-\omega$ model also provided the optimal balance between accuracy and computational cost. Calderon et al. [96] found SST $k-\omega$ overpredicted the area-averaged η_a by around 25% within the $BR < 0.15$. Wang et al. [110] reported the maximum deviation in area-averaged η_o between the simulation and experimental results was 6.9%. Similarly, Yang et al. [116] and Zhou et al. [82] revealed that the maximum relative error of area-averaged η_o was less than 6%. Sun [89] observed that the SST $k-\omega$ model was more consistent with the experimental data in the literature compared to the $k-\omega$ model, and the deviation was 3%. In short, the use of turbulence models with carefully constructed meshes depended on the validation across the experimental data to balance accuracy in transpiration cooling analysis.

Many previous studies modeled transpiration cooling using the porous-media model due to lower computational costs while maintaining accuracy [118]. Kim et al. [95] revealed a series of flow results of a C3X single-turbine blade at different studied conditions. They found that transpiration cooling formed a stable boundary layer, even with increasing coolant flow, as shown in Figure 16. At high BR , the suction-side rotating flow remained near the TE. Furthermore, transpiration cooling maintained a thick, stable coolant layer on the PS, whereas effusion cooling promoted coolant-mainstream mixing due to wake recirculation. Moreover, increasing the u_h from 2 to 20 m/s while fixing the $BR = 4.2$ showed the same trend, as compared in Figure 16a,c. In addition, a comparative analysis of transpiration cooling simulations with experimental visualization results demonstrated

excellent agreement, particularly at a low BR . This validation was further supported by Figure 16c, where simulation data closely matched the observed boundary layer development in overlapping visualizations. Under the tested conditions, the transpiration cooling maintained a thinner thermal boundary layer compared to effusion cooling [73].

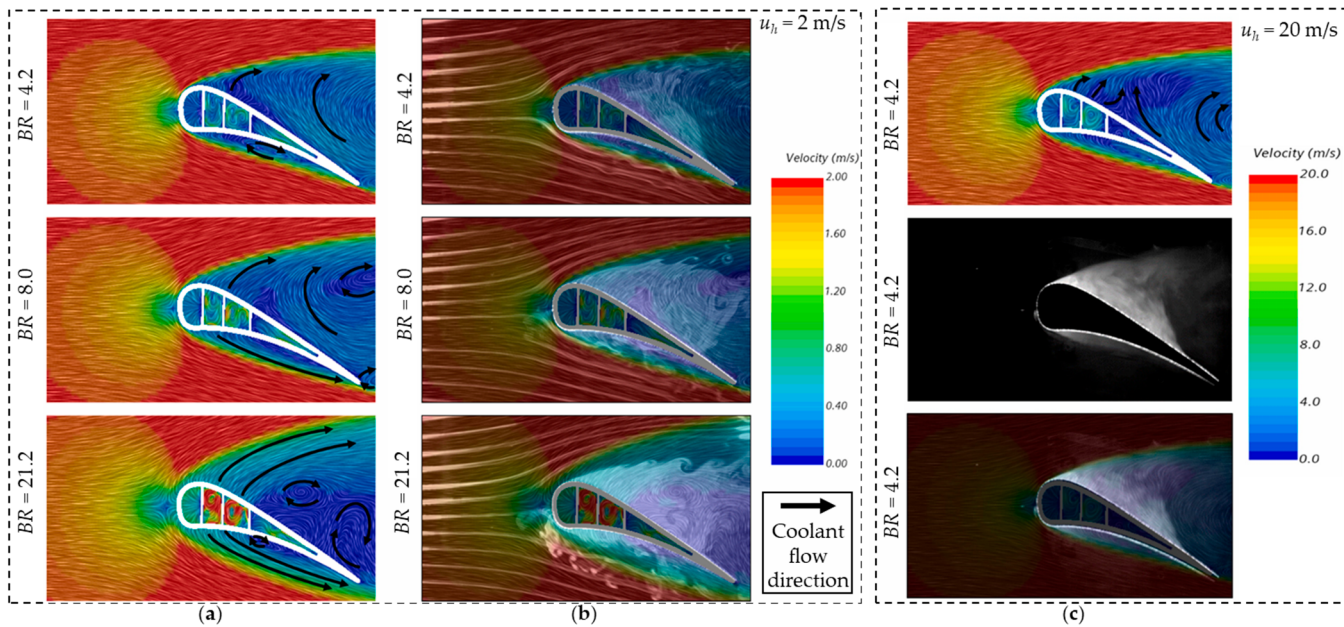


Figure 16. Flow characteristics of a C3X single-turbine transpiration-cooled blade: (a) Numerical results at $u_h = 2 \text{ m/s}$; (b) Comparison between visualization and numerical results at $u_h = 2 \text{ m/s}$; (c) Numerical results, visualized coolant flow images and comparison between visualization and numerical results at $u_h = 20 \text{ m/s}$. Reproduced with permission from [95]. Copyright 2022 Elsevier.

Kim et al. [30] also simulated the effusion and transpiration-cooled blades. The visualization results showed that for effusion and transpiration cooling, the coolant outflow formed a thinner boundary layer compared to the single blade. This thinner layer shifted the suction-side vortex rearward, reducing mainstream/coolant mixing and stabilizing the coolant within the boundary layer. Consequently, the cascade arrangement enhanced cooling performance over a single blade due to inter-blade flow interactions. Moreover, the temperature field analysis in Figure 17 revealed that the high flow resistance of the porous-media transpiration-cooled structure significantly reduced mainstream inflow compared to effusion cooling, enabling a more stable formation of cooler internal air and thermal boundary layers. Consequently, transpiration cooling outperformed effusion cooling for both single and cascade blades.

In a related study, Ma et al. [25] focused on the effects of coolant mass flow ratio and the non-uniform φ of C3X cascade-turbine blades, validated with the experimental results of Kim et al. [30]. They concluded that increasing the coolant mass flow rate enhanced the area-averaged η_o of the blade; however, the PS caused lower values compared to the SS due to mainstream flow intrusion, particularly at a high $\varphi = 80\%$. Along the coolant flow path, as pressure losses approached 100%, coolant flow stagnated, which inadequately cooled the TE. Notably, adopting a gradient φ distribution improved blade surface temperature uniformity and increased area-averaged η_o by 13.97% over conventional uniform φ designs.

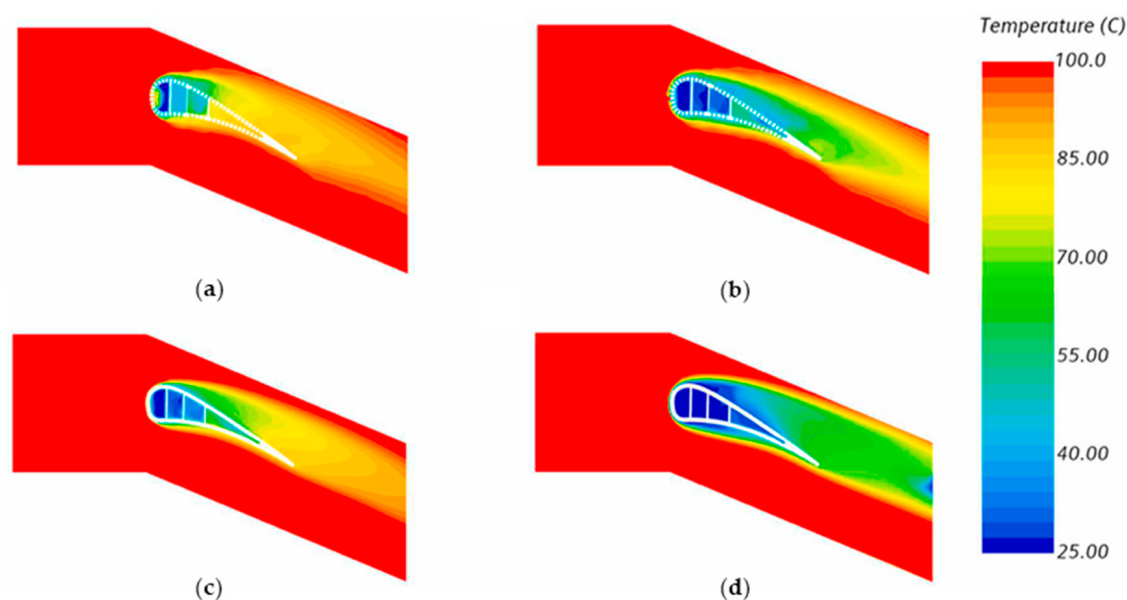


Figure 17. Temperature field of a C3X cascade-turbine transpiration-cooled blade at $u_h = 20$ m/s: (a) Effusion cooling with a volume flow rate of 100 LPM; (b) 300 LPM; (c) Transpiration cooling with a volume flow rate of 100 LPM; and (d) 300 LPM. Reproduced with permission from [30]. Copyright 2022 Elsevier.

Numerical studies have demonstrated the effectiveness of simplified computational methods for analyzing custom-designed transpiration cooling systems. Calderon et al. [96] adopted periodic boundary conditions to reduce the computational domain of a complex transpiration-cooled leading edge. The numerical model provided similar trends of area-averaged η_o and pressure loss to the experiments. Similarly, Fier et al. [100] demonstrated that a 2D RANS simulation effectively captured the essential physics of the wire-mesh transpiration-cooled plate, highlighting the relative simplicity of modeling this technique.

The geometric design of the transpiration cooling shows strong influences on cooling performance. Wang et al. [110] evaluated transpiration-cooled plates with different outlet angles and patterns, revealing that while outlet angles strongly affected temperature uniformity, they only slightly affected cooling efficiency. Complementary work by Zhou et al. [82] revealed that coolant flow resistance in the TPMS-based transpiration cooling was primarily governed by pore throat geometry, though higher resistance did not require greater injection pressure due to mainstream-coolant interactions. The study also identified that counter-rotating vortex pairs (CRVPs) in the coolant film can elevate surface skin friction, but this effect can be mitigated by complex outflow angles.

Several investigations have highlighted jet lift-off challenges in transpiration cooling. Huang et al. [51] simulated the 0.25 mm perforated transpiration-cooled plates with different partitional wall designs and found major jet lift-off in the case with the largest partition walls. This phenomenon was further explored by Yang et al. [111,112], who modeled random pore blockage effects on 200 cases of transpiration cooling and confirmed that a high plugging probability (γ) caused a significant jet lift-off, decreasing cooling effectiveness, as shown in Figure 18.

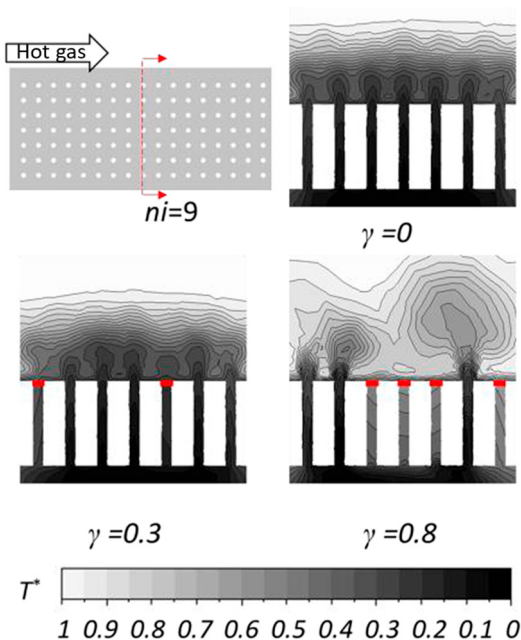


Figure 18. Simulation results showing jet lift-off of perforated transpiration-cooled plates with different pore blockage conditions. Reproduced with permission from [112]. Copyright 2018 Elsevier.

Nearly aero-engine conditions, where the T_h is above 1000 K, have also been simulated to study the impact of the φ and pressure gradient on cooling performance. Huang and He [115] used conjugate heat transfer to analyze the effect of non-uniform φ on perforated transpiration-cooled plates, where the hole diameter was varied to obtain a non-uniformity of 0–50%. Studies concluded that inhomogeneous φ had a significant influence on the cooling effects of the surface film and internal holes. Yang et al. [116] investigated transpiration cooling ($d = 0.2$ mm) with different φ configurations under varying mainstream pressure gradients. It was found that transpiration cooling outperforms film cooling by up to 100% in effectiveness, but non-uniform coolant distribution reduces efficiency. Li et al. [117] compared the cooling performance between 3D-printable swirl-chamber transpiration and the 30°–90° inclined film holes in a Can-type combustion chamber, considering chemical reactions. They concluded that hybrid cooling was highly effective for combustor liners, recommending smaller inclination angles and compound angles opposing the swirling flow for optimal performance. These studies demonstrated that advanced cooling designs significantly enhanced thermal performance under near-engine conditions, though coolant uniformity remained a key challenge for optimization.

4.5. Effect of Studied Conditions

Most studies agree that increasing coolant supply (MFR , BR or F) generally enhances cooling effectiveness, as shown in Figures 9–17. In addition, the arrangement of the perforated holes also altered the cooling effectiveness, as seen in Figure 19. However, excessive coolant flow can degrade performance. Min et al. [99] observed reduced η_a at $BR > 0.25$ due to hot gas entrainment, while Sun et al. [89] found that increasing the F from 0.2% to 1% reduced the cooling rate from 0.72 to 0.09. They solved these issues by a double coolant supply chamber, which could simultaneously improve η_o and reduce coolant consumption in perforated plate designs.

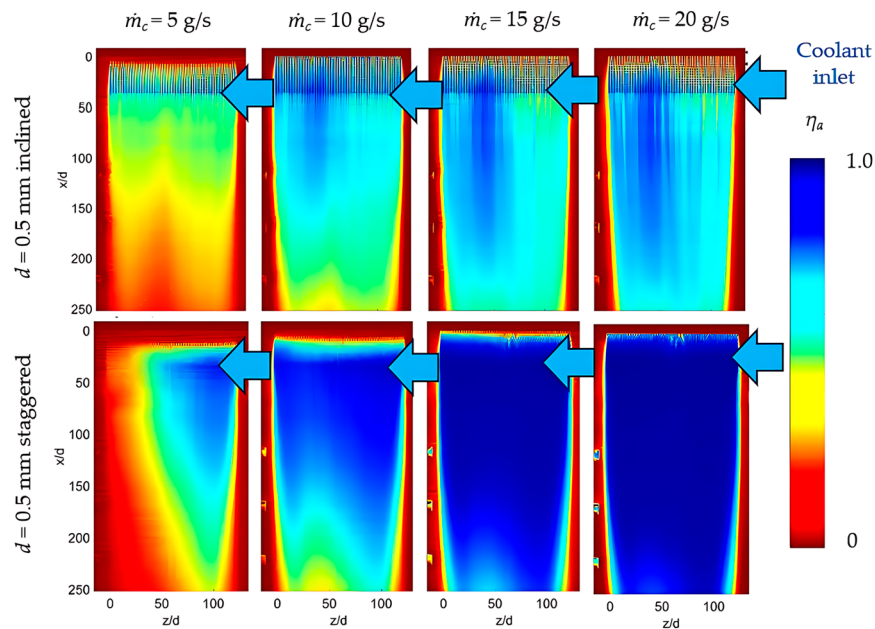


Figure 19. Influence of coolant supply and hole arrangement of transpiration cooling structures on cooling effectiveness. This figure is reproduced from [97] under a Creative Commons Attribution (CC BY) license.

Thermal resistance plays a critical role in altering the cooling effectiveness. Huang et al. [51] found that the 3D-printed transpiration-cooled plate, which was fully melted particles, enabled efficient heat conduction from the upstream to the downstream region. Therefore, it exhibited a more uniform η_o distribution and provided a slightly higher area-averaged η_o , particularly at a low F , than the sintered porous plate. This was because the sintered model had a much lower effective thermal conductivity than its bulk material [119], leading to poorer downstream cooling performance. Sun et al. [89] showed that higher Biot numbers degraded temperature uniformity due to increased thermal resistance, particularly at low thermal conductivity.

Meanwhile, Huang and He [115] showed that higher thermal conductivity in solids significantly mitigated inhomogeneous φ effects, as compared to the variation in plate thickness and hole spacing. Also, the inhomogeneous φ strongly affected η_o when a low-conductivity TBC was applied. The thin TBC layer introduced substantial thermal resistance, and lower conductivity worsened inhomogeneous φ effects. Yang et al. [116] further highlighted that under varying mainstream pressure gradients, the small spacing case and streamwise-decreasing φ model provided high cooling effectiveness and improved uniformity. Also, higher pressure gradients increased η_o and uniformity.

In short, these studies showed the need for careful design balancing coolant flow, thermal conductivity, and pore geometry in the AM-fabricated transpiration cooling systems to achieve maximum performance while mitigating jet lift-off and thermal resistance.

4.6. Effect of Structural Designs

4.6.1. Influence of Porosity

Many studies have demonstrated that porosity (φ) is critical in the performance of AM-fabricated transpiration cooling systems. Fantozzi et al. [75] observed that higher-porosity AM porous media exhibited lower discharge coefficients (CDs), highlighting the trade-off between φ and flow efficiency. In an early study, Huang et al. [49] investigated perforated transpiration cooling with hole diameters of 0.5 mm and 1 mm, fabricated by the electric spark method, finding that smaller holes ($d = 0.5$ mm) with $\varphi = 19.6\%$

achieved an area-averaged η_o comparable to sintered porous media with $\varphi = 36\%$. However, larger holes ($d = 1 \text{ mm}$) reduced the area-averaged η_o due to the enhanced mixing and boundary layer momentum at $F > 2\%$. Huang et al. [51] later revealed that as the area of the reinforcing partition walls of AM transpiration-cooled plates increased (decreasing φ), the area-averaged η_o was slightly decreased within $F = 2\text{--}3\%$.

The relationship between φ and η has been extensively studied. Broumand et al. [92] found that the Diamond TPMS transpiration-cooled plate with $\varphi = 50\%$ provided the highest η_a up to 0.75 at $F = 1.6\%$, without any jet lift-off effects. Also, even a $\varphi = 30\%$ provided $\eta_a = 0.36$ at $F = 0.68\%$, higher than conventional effusion cooling by 1.8 times. Smaller hole diameters ($d = 0.3 \text{ mm}$) were shown to enhance uniformity, with staggered hole patterns providing better performance than inclined configurations [77,89]. Wambersie et al. [97] also showed that decreasing the hole spacing on a turbine blade SS (increasing φ from 20% to 30%) significantly improved film coverage, demonstrating interactions between adjacent films and mainstream flow. However, Yang et al. [116] noted that while increasing φ generally improves area-averaged η_a , reaching up to 0.83, it can lead to non-uniform coolant distribution.

Graded and non-uniform φ distributions have emerged as promising strategies for optimizing cooling performance. Cheng et al. [64] demonstrated that IWP(A)-TPMS structures with graded φ improved coolant distribution and reduced hot-spot temperatures under non-uniform heat flux. Similarly, Ma et al. [25] proposed a φ gradient from the LE to TE of turbine blades to balance coolant seepage and prevent mainstream intrusion, as shown in Figure 20. Their findings revealed that excessive $\varphi = 80\%$ led to uneven pressure distribution and coolant leakage, emphasizing the importance of controlled φ variation.

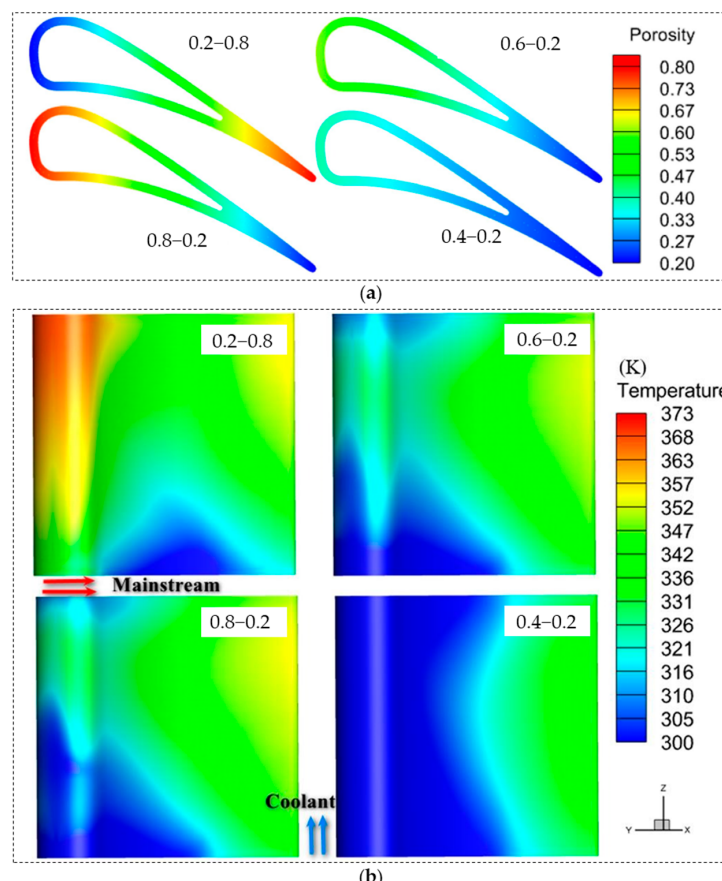


Figure 20. Non- φ distributions of the transpiration-cooled blade: (a) the distribution according to the dimensionless distance from the LE and (b) temperature contours on the blade surface. Reproduced with permission from [25]. Copyright 2023 Elsevier.

Inhomogeneous φ and manufacturing tolerances also significantly impact cooling efficiency. Huang and He [115] showed that inhomogeneous φ , which occurred during the AM process, significantly affected the surface film and internal hole cooling, causing local efficiency variations up to 41.5% and 34.5%, respectively, at a 20% non-uniformity setting. However, area-averaged and local η_o changes were minor due to heat conduction. At a non-uniformity of 50%, local impacts increased, but area-averaged η_a differences remained small. The effect of inhomogeneous φ on effusion cooling became negligible when the precision of the AM hole was maintained within a 20% variation. Overall, optimization of the φ is crucial for AM transpiration cooling systems. Graded φ designs with precise manufacturing could be a key candidate for achieving optimal coolant coverage and thermal performance in gas turbines.

4.6.2. Influence of Topology

Experimental and numerical studies have revealed that topological design critically influences the cooling effectiveness and uniformity of AM-fabricated transpiration cooling. Biomimetic approaches show particular promise, with Min et al. [76] demonstrating that blood vessel-inspired structures outperformed conventional round holes despite lower internal surface area ratios (R_{int}). This design achieved superior cooling through enhanced internal flow interaction and more uniform outlet distribution. Similarly, Sun et al. [113] reported that with the same A_{eff} , a tree-like channel achieved higher cooling efficiency than round-hole designs at equal coolant flow rates. However, Poupinha et al. [74] revealed that the unfavorable 90° ejection angle of a porous transpiration-cooled plate caused low η_a , requiring optimization of the AM build direction.

Lattice-based cooling structures exhibit significant performance variations based on their geometric configuration. Chyu et al. [78] observed that the different lattices in a transpiration-cooled plate altered the cooling performance, particularly at a $BR > 0.25$. It was observed that the η_o follows this trend: face-centered cubic > octahedral cubic \approx body-centered cubic > Kagome. Related studies on this topic indicated that the TPMS lattices presented unique advantages for transpiration-cooling applications [46]. Zhou et al. [82] found that the IWP(B) TPMS-based transpiration cooling demonstrated an optimal balance between injection pressure and cooling performance. The Primitive(B) provided superior temperature uniformity due to reduced coolant transport along the mainstream, while the IWP(A) was the preferred choice when minimizing skin friction was critical, as it effectively suppressed CRVP formation across studied flow rates. Son et al. [81] observed that surface trough orientation and internal flow path tortuosity significantly affected the η_a . They found that the Koch model with higher tortuosity minimized orientation sensitivity, achieving uniform coolant distribution, which was only 3–5% sensitivity across flow rates, while low-tortuosity Diamond exhibited strong orientation dependence up to 15–24%. Meanwhile, the Gyroid, with moderate tortuosity, showed intermediate sensitivity of 12–17%. The Koch robustness to flow direction makes it ideal for complex surfaces with directional flows.

Findings from a similar investigation revealed that the shape of cooling holes substantially influenced thermal protection characteristics. Wang et al. [110] reported that transpiration-cooled plates ($d = 0.2$ mm, $\varphi = 18.8\%$) with synclastic outlet angles improved cooling performance over reverse angles, while elliptical holes demonstrated an interesting trade-off between cooling efficiency and temperature uniformity based on their alignment with the mainstream flow. These findings emphasized the importance of hole geometry design for optimized transpiration cooling structures.

4.7. Optimization Studies

Recent advances in AM technologies have enabled innovative optimization approaches for transpiration cooling in gas turbines. The recent optimization studies can be categorized based on their methodologies and findings as follows:

4.7.1. Topology Optimization with Lattices

Yeranee et al. [18] showed that the topology-optimized cooling design incorporating TPMS lattices enhanced double-wall channel performance. The optimized design achieved a 9.5–12.5% enhancement in impingement heat transfer and 4.2–4.6% higher overall cooling effectiveness compared to pin fin configurations while simultaneously reducing pressure losses. They also demonstrated that TPMS-based topology optimization can address thermal challenges in advanced turbine cooling applications. This method could be used to avoid the footprint blockages on transpiration holes found in previous studies [78].

4.7.2. Machine Learning and Convolution-Based Modeling

Yang et al. [112] pioneered the use of convolution modeling to predict transpiration cooling and its associated plugging disadvantages, offering a quantitative understanding of random plugging effects and supporting optimization efforts, particularly in AM transpiration cooling, which held significant potential for mitigating plugging issues. Later, a novel convolution-based modeling approach for predicting η_o distributions was developed by treating the transpiration-cooled plates as void/solid logic functions [120]. Using conjugate CFD data from simple perforated transpiration-cooled plates for training, the high-resolution convolution model successfully reconstructed η_o for both training cases, achieving 4.04% error within 100 training steps and more complex validation geometries. They claimed that the method significantly reduced parameter space dimensionality while preserving physical interactions between coolant holes through an efficient initialization process using decoupled weight functions. In a more recent study, Yang et al. [121] developed a machine learning model using convolutional neural networks to predict the η_a in the perforated transpiration-cooled plates by integrating image conversion, convolution, and nonlinear activation processes. Training and validation used CFD data from regular and random film cooling hole arrays. Results showed that the model achieved few errors, less than 10% for training and 13% for validation. The convolution kernel revealed coolant superposition as a key factor in effusion cooling.

4.7.3. Surrogate Modeling and Evolutionary Algorithms

Several studies combined CFD with surrogate modeling and evolutionary algorithms for optimization. Wang et al. [122] used RANS simulations with the Brinkman–Forchheimer–Darcy model and a Kriging–genetic algorithm (GA) optimization framework for optimizing a transpiration-cooled C3X cascade-turbine blade with multiple porous zones of varying φ . The research revealed that the highest φ should be at the LE and PS for optimal cooling. A subsequent study [123] employed a multi-objective optimization of a transpiration-cooled C3X cascade-turbine blade using CFD modeling and a surrogate-based approach combining an artificial neural network (ANN) and a non-dominated sorting genetic algorithm-II (NSGA-II). The optimization framework treated φ distribution across different vane zones as design variables to balance cooling performance and aerodynamic efficiency. The results showed that the LE coolant discharge significantly enhanced cooling but increased porous-media pressure losses while maintaining consistent mainstream pressure losses, approximately 18% for all cases. They concluded that the optimal design required careful coolant allocation to the leading edge and adjacent SS and PS. Similarly, Lv et al. [27] showed that a porous-media plate beneath film holes improved cooling effectiveness by

30% compared to conventional double-wall cooling, with a further 8.5–8.7% improvement from the GA optimization.

4.7.4. Gradient Porosity and Response Surface Methods

Chen et al. [124] and Liu et al. [90] explored gradient φ designs using a response surface methodology and multi-objective genetic algorithms (MOGAs). Chen et al. [124] demonstrated that gradient φ plates improved temperature uniformity by 20.58–23.78% while reducing injection pressure by 84.5–86.2%. Liu et al. [90] developed an ANN-MOGA framework that increased cooling efficiency by 11.35% and reduced pressure loss by 36.23% compared to uniform φ designs. These studies emphasize the benefits of tailored φ distributions in achieving high-performance cooling.

5. Challenges and Future Directions

5.1. Additive Manufacturing Challenges and Innovations

The challenges of AM-fabricated film cooling have been well described by Dutta et al. [2]. They concluded that the AM film cooling surfaces reduced film effectiveness by disrupting jets but enhanced in-hole convection. Yeranee et al. [18] observed that the as-printed model exhibited partially fused powder particles adhering to the pedestal structures, effusion holes, and impingement cooling channels, as shown in Figure 21, attributed to non-optimized AM parameters and printing orientation. Post-processing, such as surface machining or chemical polishing, improved the external surface finish of the effusion and impingement plates, resulting in a relatively smooth exterior. However, high-resolution CT scans revealed the presence of internal micro-voids, particularly within the pedestal near the effusion plate, suggesting potential challenges in achieving fully dense structures with uncontrolled AM settings.

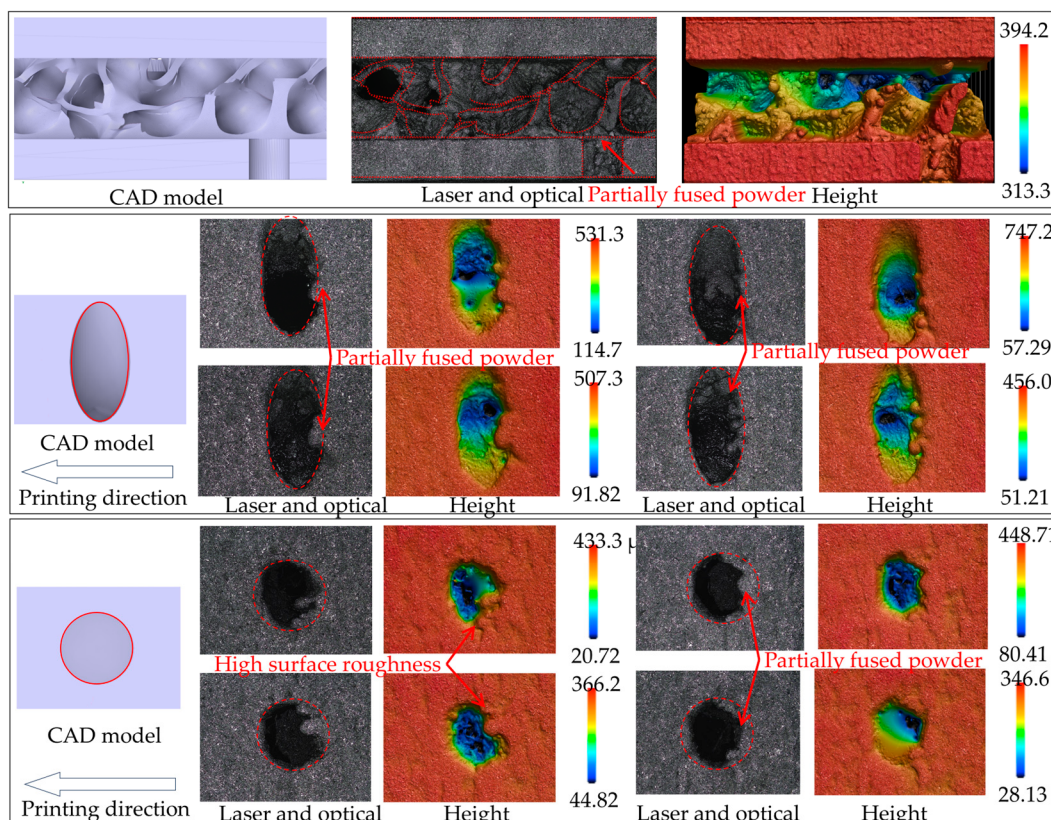


Figure 21. Deviations, defects, and surface roughness of AM-fabricated gas turbine cooling structures (unit: μm). Reproduced with permission from [18]. Copyright 2024 Elsevier.

The fabrication of transpiration cooling systems through AM technology also presents several persistent challenges that impact system performance. Dimensional accuracy issues remain prevalent, with multiple studies documenting deviations in hole sizes and φ in the AM-fabricated components. Table 5 overviews the deviations in different AM transpiration cooling designs. It can be highlighted that the etching and laser drilling obtained better accuracy than the AM methods, where most of the AM methods caused hole size and φ reduction from the designs. The SLM-produced perforations were consistently undersized compared to the design specifications, showing reductions ranging from 4% for 0.24 mm holes to 77% for 0.06 mm holes [66]. Similar findings were reported by Min et al. [76,77]. They noted that the DLMS caused φ shrinkage of about 40% for 0.3 mm holes and outlet area reduction by 27–39% for 0.5 mm holes in round-hole designs.

Table 5. Overview of deviations in different AM transpiration cooling geometries.

Ref.	Printed Geometry	Manufacturing Method (Surface Treatment)	Material	Design Values	Deviations from Designs	
[66]	Oblique cylinder hole	Etching (Polish)	Stainless steel	$d = 0.063 \text{ mm}$ pitch = 0.063 mm $\varphi = 91\%$	$d \approx -1\% \text{ to } -4\%$ pitch $\approx -1\%$ $\varphi \approx -1\% \text{ to } -7\%$	
	Truncated-cone hole	Laser drilling (Polish)		$d = 0.06\text{--}0.24 \text{ mm}$ pitch = 0.6–2.4 mm $\varphi = 91\%$	$d \approx -8\% \text{ to } -30\%$ pitch $\approx -2\% \text{ to } -5\%$ $\varphi \approx -15\% \text{ to } -48\%$	
	Round hole	SLM (Laser clean)		$d = 0.06\text{--}0.24 \text{ mm}$ pitch = 0.6–2.4 mm $\varphi = 91\%$ $d = 0.25 \text{ mm}$	$d \approx -2\% \text{ to } -37\%$ pitch $\approx -33\% \text{ to } 0.2\%$ $\varphi \approx -4\% \text{ to } -77\%$ $d \approx -0.4\% \text{ to } 17.2\%$	
[76]	Quadratic-truncated-cone hole	SLA	Resin	pitch = 2.686 mm $\varphi = 1.0\%$	$\varphi \approx -0.6\% \text{ to } -0.7\%$ $\varphi \approx -29\% \text{ to } 9\%$	
	0.3 mm-round hole (3 d -pitch)	DLMS (Heat treatment, Supporting removal, De-powdering process)		$\varphi = 4.13\%$	$\varphi \approx -39\%$	
	0.3 mm-round hole (2 d -pitch)			$\varphi = 8.15\%$	$\varphi \approx -12\%$	
	Sphere packing			$\varphi = 10.73\%$	$\varphi \approx -7.2\%$	
	Wire-mesh matrix			$\varphi = 20.89\%$	$\varphi \approx -12\%$	
	Blood vessel			$\varphi = 13.42\%$	$\varphi \approx -15\%$	
	Film cooling			$\varphi = 2.32\%$	$\varphi \approx -31\%$	
	Round hole (1.5 d -pitch)			$A_{out} = 70,685.8 \mu\text{m}^2$ $d = 0.3 \text{ mm}$	$A_{out} \approx -39\%, d \approx -22\%$	
	Round hole (2 d -pitch)				$A_{out} \approx -49\%, d \approx -28\%$	
[77]	Round hole (3 d -pitch)				$A_{out} \approx -44\%, d \approx -25\%$	
	Round hole (1.5 d -pitch)				$A_{out} \approx -36\%, d \approx -20\%$	
	Round hole (1.5 d -pitch)	DLMS (Supporting removal)	Inconel 718	$A_{out} = 125,663.7 \mu\text{m}^2$ $d = 0.4 \text{ mm}$	$A_{out} \approx -41\%, d \approx -17\%$	
	Round hole (2 d -pitch)				$A_{out} \approx -35\%, d \approx -19\%$	
	Round hole (3 d -pitch)				$A_{out} \approx -29\%, d \approx -16\%$	
	Round hole (1.5 d -pitch)			$A_{out} = 196,349.5 \mu\text{m}^2$ $d = 0.5 \text{ mm}$	$A_{out} \approx -28\%, d \approx -15\%$	
	Round hole (2 d -pitch)				$A_{out} \approx -27\%, d \approx -14\%$	
[92]	Round hole (3 d -pitch)			$\varphi = 30\%$	$\varphi = -39\%$	
	Diamond TPMS lattice	SLA	Resin	$\varphi = 40\%$	$\varphi = -24\%$	
[80]	Gyroid TPMS lattice	LPBF	Inconel 625	$\varphi = 50\%$	$\varphi = -15\%$	
				$\varphi = 61\%$	$\varphi = -1\%$	

In addition, Huang et al. [51] reported a designed 0.3 mm hole printing at 0.25 mm due to laser beam limitations and heat diffusion, while Broumand et al. [92] noted that Diamond TPMS structures consistently achieved lower φ than designed, particularly in low- φ cases. Zhang et al. [80] found that while the LPBF-fabricated TPMS structures met φ targets, surface defects reduced permeability by around 15% compared to CAD models. Ealy et al. [79] confirmed these trends through X-ray CT analysis, showing that while 95% of surfaces met 320 μm , tolerances in the SLM Inconel 718 blades feature accuracy degraded significantly beyond 60° from the build direction. These dimensional inaccuracies directly affect pressure losses and flow distribution within the cooling structures.

Process parameter optimization presents another significant challenge, as demonstrated by Fantozzi et al. [75]. They found that increasing laser power while reducing scan speed improved geometric regularity but decreased φ , consequently increasing flow resistance. Son et al. [102] further identified critical limitations in the SLA-printed Diamond TPMS plates, where φ below 10% resulted in unprintable regions with stochastic pore clogging. Surface characteristics also significantly impact performance, with SEM analyses [51,125] confirming that as-printed channels were typically 15% smaller than designed.

Huang et al. [51] noted that while adhered metal particles increased surface roughness, they enhanced heat transfer by acting as micro-fins. Min et al. [77] quantified printing accuracy through backlit imaging, finding that smaller pores ($d = 0.3$ mm) had >10% plugging versus 0% for 0.5 mm holes.

Future advancements in this area are focusing on several promising directions. Recent developments in AM-assisted casting of complex lattices [126,127] have shown the potential to match LPBF mechanical properties at reduced costs while achieving smoother surfaces. Emerging SLA, digital light processing, or liquid crystal display techniques [128–130] are enabling the fabrication of complex ceramic cores for transpiration channels, though challenges remain in achieving high green density post-sintering. Particularly noteworthy is the work of Min et al. [131], who developed an AM-processed oxide dispersion-strengthened coating via DMLS that demonstrated exceptional 1200 °C oxidation resistance over 2000 h while maintaining interfacial integrity. These advanced solutions could effectively mitigate the limitations of AM-fabricated transpiration cooling.

5.2. Pore Blockage and Mitigation Strategies

Pore blockage continues to be a critical reliability concern for transpiration cooling systems, with clogged holes potentially causing dangerous local temperature spikes and system failure [15]. Traditional sintered porous media are particularly susceptible to unpredictable dust-induced clogging, though AM techniques offer improved microscale control. Yang et al. [111] demonstrated the impact of increased pore blockage ratios in 0.4 mm perforated plates on cooling effectiveness, particularly in upstream regions.

Recent research has identified several promising approaches to mitigate these issues. Sun et al. [113] showed that at low F , the influence of pore blockage was minor in the tree-like channels, demonstrating their clogging resistance, while the maximum loss of the area-averaged η_o by 16.3% was found at $F = 2\%$. Yang et al. [114] found that the proposed oriented porous structures improved cooling performance, reduced coolant consumption at equivalent cooling performance by 10–270%, and decreased the temperature gradient, eventually minimizing thermal stress and improving the reliability of the porous transpiration cooling. Sun et al. [89] introduced double coolant supply channels and found that the nonuniform coolant distribution increased area-averaged η_o by 3.27% while improving temperature uniformity.

Future work in this area will explore hybrid cooling configurations that combine the benefits of different approaches. Ding et al. [132] demonstrated that binary porous matrices could maintain 44.5% longer effective film lengths while using 20% less coolant compared to single porous matrices. Natsui et al. [133] showed synergistic effects when coupling discrete film cooling holes with transpiration cooling, effectively mitigating detrimental vortex structures. These hybrid approaches, originally developed for aerospace applications [26,134], can be adapted for gas turbine implementations with promising results.

5.3. Mechanical Integrity and Enhanced Design Approaches

The balance between mechanical strength and cooling performance remains a key challenge for AM-fabricated transpiration cooling structures. Min et al. [77] found that while 3d-pitch straight holes had the highest stress net area, staggered holes unexpectedly exhibited lower ultimate tensile strength (UTS) due to intersecting stress concentrations [135]. Huang et al. [51] provided a comparative analysis showing AM porous samples reaching 0.95 GPa UTS with 60% blockage, representing a 440% improvement over traditional sintered materials, but the samples were still 10% weaker than solid SLM specimens.

Future directions for addressing these mechanical challenges include advanced surface engineering and post-processing techniques. Ligrani et al. [136] demonstrated that abrasive flow machining methods achieved superior smoothness compared to as-built and chemically polished surfaces. Chyu et al. [125] successfully reduced surface roughness by over 40% through redesign and electrochemical processing. Arai and Suidzu [137] developed innovative plasma-sprayed porous coatings using yttria-stabilized zirconia and polyester powder that enabled active transpiration cooling under pressure gradients while maintaining low thermal conductivity. The optimized designs, advanced surface treatments, and innovative coatings significantly improve the integrity of AM transpiration cooling for next-generation gas turbines.

5.4. Experimental and Simulation Challenges with Future Methodologies

Experimental research encountered several challenges, mainly due to the current AM limitations. Firstly, most previous studies relied on simplified flat-plate models that cannot fully replicate the real applications. Since then, there has been limited high-temperature data for gas turbines due to measurement difficulties in extreme transpiration cooling flow. Meanwhile, numerical modeling of transpiration cooling faced its own set of challenges. Current approaches to single-phase cooling simulations have often oversimplified porous structures as homogeneous fluid zones with resistance terms, decreasing flow and temperature field prediction accuracy. While more detailed geometric modeling was possible, it has prohibitively high computational costs due to the number of meshes, as seen in Table 4.

Another critical challenge in AM transpiration cooling studies lies in persistent simulation–experiment discrepancies. Calderon [96] found CFD consistently over-predicted area-averaged η_a due to imperfect decay modeling. Huang et al. [51] attributed the discrepancy between simulation and experimental results to conduction heat loss apart from the roughness of the transpiration cooling samples. Unlike the simulation, the experiment involved heat conduction from the wind tunnel wall to the porous plate, which was not accounted for in the numerical model. Kim et al. [95] reported that as the BR increased in a transpiration-cooled C3X turbine blade, the simulated coolant film became larger than in the visualization due to resistance from the dense cooling air mixed with olive oil droplets. Yang et al. [121] found in their machine learning model that even though the method reduces computational costs and provides 2D cooling effectiveness distributions, it lacks internal cooling performance and universality for broader design applications.

Future experimental methodologies are addressing these limitations through advanced diagnostic techniques. Greifenstein et al. [76] revealed critical flame-cooling interactions in effusion-cooled combustors, where low-swirl premixed flames intensified thermal coupling. The wall temperature variations reached 150–200 K, corresponding to an area-averaged $\eta_a = 0.45\text{--}0.62$. For transpiration cooling, these findings suggested that swirl management was essential to mitigate hot spots. Also, optical diagnostics, such as hydroxyl radical, coherent anti-Stokes Raman spectroscopy, and thermographic phosphors, can validate transpiration cooling effectiveness in reacting flows. Moreover, the coolant injection strategies must account for combustion-driven thermal gradients.

High-fidelity simulations, such as LES, and rotation effect modeling are essential for the next numerical studies on transpiration cooling. Xiao et al. [138] used LES/Darcy–Forchheimer modeling to reveal Kelvin–Helmholtz jelly roll instabilities, which are critical for predicting mainstream mixing. You et al. [139] found that rotation reduced target-surface cooling efficiency, mainly due to the effects of Coriolis, buoyancy, centrifugal forces, and pressure gradient that deflected the jet impingement. For reactor conditions, Zhang et al. [140] proposed a local thermal non-equilibrium (LTNE) model for gaseous transpiration cooling, incorporating radiation via Rosseland approximation and gas expansion

effects via low Mach approximation. These studies were highly relevant for gas turbine transpiration cooling, as they addressed vortex-resolved flow prediction, rotational effects, high-temperature radiation effects, coolant expansion, and pumping power optimization.

5.5. Integrated Optimization Approaches

Future advancements in transpiration cooling for gas turbine blades will increasingly rely on AI-driven optimization techniques such as ANN combined with MOGA [90,123] to design optimized non-stochastic cooling structures. Recent work shows that topology optimization combining RANS and porous-media modeling [141] effectively captures fluid-porous interactions, while meshless TPMS methods proposed by Jiang et al. [142] enable graded- φ designs with desired mechanical integrity. Though requiring improved multi-physics modeling, these approaches can revolutionize transpiration cooling by optimizing thermal protection, structural integrity, and aerodynamic efficiency simultaneously. Their integration will be key for future engines operating under extreme conditions.

6. Conclusions

Transpiration cooling, enhanced by additive manufacturing (AM), offers superior thermal management for gas turbines through complex and high-performance porous structures. This review analyzes its evolution, flow/heat transfer mechanisms, and experimental/numerical progress, demonstrating its advantages over conventional methods. However, key challenges remain, requiring advanced solutions to ensure the usability of AM transpiration cooling for practical gas turbines. The conclusions are drawn as follows:

1. AM-fabricated perforated transpiration-cooled plates achieve 10–100% higher cooling effectiveness than traditional film cooling, though dimensional inaccuracies around 4–77% porosity shrinkage in 0.06–0.5 mm holes and 10% ultimate tensile strength reductions in AM models present reliability concerns. While the integration of CAD-based lattice structures with transpiration cooling slightly reduces cooling performance, it mitigates pore blockage effects and provides superior structural support, overcoming the mechanical limitations of pure transpiration cooling.
2. Advanced AM techniques allow the precise fabrication of complex and deterministic structures, such as TPMS and biomimetic designs. These cooling models enhance adiabatic cooling effectiveness by up to five times compared to conventional film cooling. Gradient porosity/thickness of such structures balances thermal-mechanical properties, mitigates jet lift-off, and provides flow uniformity, improving temperature distributions on the surface.
3. Transpiration cooling forms a more stable boundary layer on the hot wall than effusion cooling, particularly on the blade surface, but excessive coolant supply can degrade performance due to hot gas entrainment. Precise control of the porosity and coolant supply is therefore required to avoid coolant leakages, non-uniform coolant distributions, and uneven temperature/pressure patterns.
4. Current AM technology introduces 15% hole size reductions from surface roughness and around 15% permeability deviations from CAD models, compounded by unresolved high-temperature material limitations, with only direct metal laser sintering (DMLS)-fabricated oxide coatings demonstrating reliable stability.
5. AI-driven optimization, such as artificial neural networks (ANNs) combined with multi-objective genetic algorithms (MOGAs), topology optimization, and hybrid cooling, such as discrete film holes with transpiration cooling, also offer balanced thermal-structural solutions. Nonetheless, their implementation requires advanced experimental diagnostics and high-fidelity multiphysics modeling to fully validate these innovative cooling systems for practical implementation.

Overcoming the challenges presented in this review could redefine gas turbine thermal management, enabling high-efficiency engines. Therefore, the integration of advanced AM, multiphysics validation from high-fidelity simulations and experiments, AI-driven optimization, and hybrid cooling for transpiration cooling promises revolutionary advances in gas turbine cooling technologies.

Author Contributions: Conceptualization, K.Y. and Y.R.; formal analysis, K.Y.; writing—original draft preparation, K.Y.; writing—review and editing, K.Y. and Y.R.; supervision, Y.R.; project administration, K.Y. and Y.R.; methodology, K.Y.; funding acquisition, K.Y. and Y.R. All authors have read and agreed to the published version of the manuscript.

Funding: This work received financial support through the National Science and Technology Major Project (2017-III-0009-0035) and National Natural Science Foundation of China (24Z033103800, 11972230), with additional technical support from the Chinese-German Joint Cooperation Group (GZ1577) program.

Data Availability Statement: The original contributions presented in this study are included in the article. Further inquiries can be directed to the corresponding author.

Acknowledgments: The authors would like to express their deepest gratitude to Sunanta Yeranee and Pornpana Sarawong for their encouragement throughout this research. Special thanks also go to our labmates at the Institute of Turbomachinery, School of Mechanical Engineering, Shanghai Jiao Tong University, China, for their invaluable support during the preparation of this work. Their collective strength and inspiration have been instrumental in my study.

Conflicts of Interest: The authors declare no conflicts of interest.

Nomenclature

A_{eff}	Coolant covered area on the hot-side surface (m^2)
A_h	Cross-sectional area of the mainstream channel (m^2)
A_{int}	Internal area of the solid–fluid interface inside the specimens (m^2)
A_{out}	Outlet area of the coolant at the outer surface (m^2)
A_{pore}	Total cross-sectional area of transpiration cooling topology (m^2)
Bi	Biot number (-)
BR	Blowing ratio (-)
CD, CF	Discharge and skin-friction coefficients (-)
C_F	Inertial resistance coefficient ($1/\text{m}$)
C_h	Circumference of the mainstream channel (m)
c_p	Heat capacity of the fluid ($\text{J}/(\text{kg}\cdot\text{K})$)
d_c, d_h	Hydraulic diameter of coolant and mainstream channels (m)
d, d_{pore}	Diameter of micro hole and porous-media pore (m)
F	Injection ratio (-)
F	External force in Navier–Stokes equation (N/m^3)
h	Convective heat transfer coefficient ($\text{W}/(\text{m}^2\text{K})$)
k	Turbulence kinetic energy in turbulence model (m^2/s^2)
K	Permeability (m^2)
k_{eff}	Effectiveness thermal conductivity of porous media ($\text{W}/(\text{m}\cdot\text{K})$)
k_f, k_s	Thermal conductivity of fluid and solid ($\text{W}/(\text{m}\cdot\text{K})$)
L	Unit cell size (m)
L_c	Characteristic length of the transpiration cooling design (m)
\dot{m}_c, \dot{m}_h	Mass flow rate of coolant and mainstream (kg/s)
Ma	Mach number (-)
MFR	Mass flow ratio of coolant to mainstream (-)
Nu	Nusselt number (-)
Nu/Nu_0	Normalized Nusselt number for heat transfer enhancement evaluation (-)

p	Pressure field (Pa)
$p_{t,in}, p_{t,out}$	Total pressure of the coolant inlet and outlet (Pa)
$q(x)$	Heat flux (W/m^2)
Q_{tot}	Total heat transfer (W)
R_{int}, R_{out}	Internal and outlet area ratios (-)
Re_c, Re_h	Reynolds number of coolant and mainstream (-)
S_m	Mass source term (N/m^3)
S_v	Specific surface area ($1/\text{m}$)
t	Thickness (m)
T^*	Non-dimensional temperature (-)
T_c, T_h, T_s	Coolant, mainstream and surface temperatures (K)
T_{flu}, T_{sol}	Temperature of fluid and solid (K)
\mathbf{u}	Velocity vector (m/s)
u_c, u_h, u_D	Coolant, mainstream and Darcy velocities (m/s)
\dot{V}	Volumetric flow rate (liters per minute: LPM)
V_{des}	Design volume from CAD models (m^3)
V_{sol}	Volume of solid domain with identical dimension (m^3)
v_c	Average velocity of coolant flow in the film hole or pore (m/s)
x, y, z	Cartesian coordinate (-)
Greek letters	
γ	Plugging probability (-)
ε	Turbulent dissipation rate (m^2/s^3)
ζ_{Pt}	Total pressure loss coefficient (-)
η_a, η_o	Adiabatic and overall cooling effectiveness (-)
μ	Dynamic viscosity of fluid ($\text{kg}/(\text{m}\cdot\text{s})$)
ρ_c, ρ_h	Fluid density of coolant and mainstream (kg/s)
τ_w	Shear stress (Pa)
φ	Porosity (%)
$\varphi_{des}, \varphi_{act}$	Design and actual porosities (%)
ω	Specific dissipation rate in turbulence model (1/s)
Abbreviations	
ANN	Artificial neural network
AM	Additive manufacturing
CAD	Computer-aided design
CCD	Charged-coupled device
CFD	Computational fluid dynamics
CMC	Ceramic matrix composite
CRVP	Counter-rotating vortex
CT	Computed tomography
DLD	Direct laser deposition
DMLS	Direct metal laser sintering
EOS	Electro Optical Systems
FDM	Fused deposit modeling
GA	Genetic algorithm
IR	Infrared thermography
IWP	I-graph and wrapped package
LES	Large eddy simulation
LBM	Lattice Boltzmann method
LTNE	Local thermal non-equilibrium
MIM	Metal powder injection molding
MOGA	Multi-objective genetic algorithms
NASA	National Aeronautics and Space Administration
NS	Navier-Stokes
NSGA-II	Non-dominated sorting genetic algorithm-II

OH-PLIF	Hydroxyl radical
PVD	Physical vapor deposit
PIV	Particle image velocimetry
PS	Pressure side of turbine blades
PSP	Pressure-sensitive paint
RANS	Reynolds-averaged Navier–Stokes
SLA	Stereolithography
SLM	Selective laser melting
SS	Suction side of turbine blades
TE	Trailing edge
TBC	Thermal barrier coating
TIT	Turbine inlet temperature
TKE	Turbulence kinetic energy
TLC	Transient liquid crystal thermography
TPMS	Triply periodic minimal surface
UTS	Ultimate tensile strength (Pa)

References

1. Perepezko, J.H. The Hotter the Engine, the Better. *Science* **2009**, *326*, 1068–1069. [[CrossRef](#)]
2. Dutta, S.; Kaur, I.; Singh, P. Review of Film Cooling in Gas Turbines with an Emphasis on Additive Manufacturing-Based Design Evolutions. *Energies* **2022**, *15*, 6968. [[CrossRef](#)]
3. Ishikawa, M.; Komori, T.; Terauchi, M.; Yasuraoka, J. Development of High Efficiency Gas Turbine Combined Cycle. *Tech. Rev. Mitsubishi Heavy Ind.* **2008**, *45*, 15–17.
4. Hada, S.; Tsukagoshi, K.; Masada, J.; Ito, E. Test Results of the World’s First 1600 °C J-Series Gas Turbine. *Mitsubishi Heavy Ind. Tech. Rev.* **2012**, *49*, 18–23.
5. Wang, W.; Yan, Y.; Zhou, Y.; Cui, J. Review of Advanced Effusive Cooling for Gas Turbine Blades. *Energies* **2022**, *15*, 8568. [[CrossRef](#)]
6. Han, J.-C.; Dutta, S.; Ekkad, S. *Gas Turbine Heat Transfer and Cooling Technology*, 2nd ed.; CRC Press: Boca Raton, FL, USA, 2012; ISBN 9780429107115.
7. Clarke, D.R.; Oechsner, M.; Padture, N.P. Thermal-Barrier Coatings for More Efficient Gas-Turbine Engines. *MRS Bull.* **2012**, *37*, 891–898. [[CrossRef](#)]
8. Li, Y.; Rao, Y.; Wang, D.; Zhang, P.; Wu, X. Heat Transfer and Pressure Loss of Turbulent Flow in Channels with Miniature Structured Ribs on One Wall. *Int. J. Heat Mass Transf.* **2019**, *131*, 584–593. [[CrossRef](#)]
9. Liang, C.; Rao, Y. Computational Analysis of Rotating Effects on Heat Transfer and Pressure Loss of Turbulent Flow in Detached Pin Fin Arrays with Various Clearances. *ASME J. Heat Transf.* **2020**, *142*, 121803. [[CrossRef](#)]
10. Rao, Y.; Feng, Y.; Li, B.; Weigand, B. Experimental and Numerical Study of Heat Transfer and Flow Friction in Channels With Dimples of Different Shapes. *J. Heat Transfer* **2015**, *137*, 031901. [[CrossRef](#)]
11. YERANEE, K.; RAO, Y. A Review of Recent Studies on Rotating Internal Cooling for Gas Turbine Blades. *Chinese J. Aeronaut.* **2021**, *34*, 85–113. [[CrossRef](#)]
12. Babji, G.; Pujari, A.K. Flow and Heat Transfer Studies of Multijet Impingement Cooling for Different Configurations: A Review. *Heat Transf.* **2022**, *52*, 1604–1672. [[CrossRef](#)]
13. Ahn, J. Large Eddy Simulation of Film Cooling: A Review. *Energies* **2022**, *15*, 8876. [[CrossRef](#)]
14. Nealy, D.A.; Reider, S.B. Evaluation of Laminated Porous Wall Materials for Combustor Liner Cooling. *J. Eng. Gas Turbines Power* **1980**, *102*, 268–276. [[CrossRef](#)]
15. Wassell, A.B.; Bhangu, J.K. The Development and Application of Improved Combustor Wall Cooling Techniques. In *Turbo Expo: Power for Land, Sea, and Air*; American Society of Mechanical Engineers: New York, NY, USA, 1980; pp. 1–10.
16. Murray, A.V.; Ireland, P.T.; Romero, E. Experimental and Computational Methods for the Evaluation of Double-Wall, Effusion Cooling Systems. *J. Turbomach.* **2020**, *142*, 111003. [[CrossRef](#)]
17. Li, W.; Lu, X.; Li, X.; Ren, J.; Jiang, H. On Improving Full-Coverage Effusion Cooling Efficiency by Varying Cooling Arrangements and Wall Thickness in Double Wall Cooling Application. *J. Heat Transfer* **2019**, *141*, 042201. [[CrossRef](#)]
18. Yeranee, K.; Rao, Y.; Xu, C.; Xie, J.; Zhang, Y. Conjugate Heat Transfer and Fluid Flow Analysis on Printable Double-Wall Effusion Cooling with Internal Topology-Optimized TPMS Structures. *Therm. Sci. Eng. Prog.* **2024**, *55*, 102939. [[CrossRef](#)]

19. Rao, Y.; Liu, Y.; Wan, C. Multiple-Jet Impingement Heat Transfer in Double-Wall Cooling Structures with Pin Fins and Effusion Holes. *Int. J. Therm. Sci.* **2018**, *133*, 106–119. [[CrossRef](#)]
20. Skamniotis, C.; Cocks, A.C.F. Minimising Stresses in Double Wall Transpiration Cooled Components for High Temperature Applications. *Int. J. Mech. Sci.* **2021**, *189*, 105983. [[CrossRef](#)]
21. Skamniotis, C.; Courtis, M.; Cocks, A.C.F. Multiscale Analysis of Thermomechanical Stresses in Double Wall Transpiration Cooling Systems for Gas Turbine Blades. *Int. J. Mech. Sci.* **2021**, *207*, 106657. [[CrossRef](#)]
22. Skamniotis, C.; Cocks, A.C.F. Designing against Severe Stresses at Compound Cooling Holes of Double Wall Transpiration Cooled Engine Components. *Aerospace Sci. Technol.* **2021**, *116*, 106856. [[CrossRef](#)]
23. Courtis, M.; Skamniotis, C.; Cocks, A.; Ireland, P. Coupled Aerothermal-Mechanical Analysis in Single Crystal Double Wall Transpiration Cooled Gas Turbine Blades with a Large Film Hole Density. *Appl. Therm. Eng.* **2023**, *219*, 119329. [[CrossRef](#)]
24. Liang, C.; Rao, Y.; Luo, J.; Luo, X. Experimental and Numerical Study of Turbulent Flow and Heat Transfer in a Wedge-Shaped Channel with Guiding Pin Fins for Turbine Blade Trailing Edge Cooling. *Int. J. Heat Mass Transf.* **2021**, *178*, 121590. [[CrossRef](#)]
25. Ma, H.; Sun, H.; Fu, H.; Luan, Y.; Sun, T.; Zunino, P. Numerical Investigation on Transpiration Cooling Performance of Turbine Blades with Non-Uniform Porosity. *Appl. Therm. Eng.* **2023**, *235*, 121394. [[CrossRef](#)]
26. Jiang, P.X.; Huang, G.; Zhu, Y.; Liao, Z.; Huang, Z. Experimental Investigation of Combined Transpiration and Film Cooling for Sintered Metal Porous Struts. *Int. J. Heat Mass Transf.* **2017**, *108*, 232–243. [[CrossRef](#)]
27. Lv, Y.; Liu, T.; Huang, X.; He, F.; Tang, L.; Zhou, J.; Wang, J. Numerical Investigation and Optimization of Flat Plate Transpiration-Film Combined Cooling Structure. *Int. J. Therm. Sci.* **2022**, *179*, 107673. [[CrossRef](#)]
28. Munk, D.J.; Selzer, M.; Seiler, H.; Ortelt, M.; Vio, G.A. Analysis of a Transpiration Cooled LOX/CH₄ Rocket Thrust Chamber. *Int. J. Heat Mass Transf.* **2022**, *182*, 121986. [[CrossRef](#)]
29. Steingrimsson, A.; Marsell, B.; Mankbadi, R.; Kapat, J. Towards Prediction of Transpiration Cooling. In Proceedings of the 48th AIAA Aerospace Sciences Meeting Including the New Horizons Forum and Aerospace Exposition, Orlando, FL, USA, 4–7 January 2010. [[CrossRef](#)]
30. Kim, M.; Shin, D.H.; Lee, B.J.; Lee, J. Experimental and Numerical Investigation of Micro-Scale Effusion and Transpiration Air Cooling on Cascaded Turbine Blades. *Case Stud. Therm. Eng.* **2022**, *32*, 101892. [[CrossRef](#)]
31. Song, K.D.; Choi, S.H.; Scotti, S.J. Transpiration Cooling Experiment for Scramjet Engine Combustion Chamber by High Heat Fluxes. *J. Propuls. Power* **2006**, *22*, 96–102. [[CrossRef](#)]
32. Elnady, T.; Hassan, I.; Kadem, L.; Lucas, T. Cooling Effectiveness of Shaped Film Holes for Leading Edge. *Exp. Therm. Fluid Sci.* **2013**, *44*, 649–661. [[CrossRef](#)]
33. Reimer, T.; Kuhn, M.; Gülan, A.; Esser, B.; Sippel, M.; Foreest, A. Van Transpiration Cooling Tests of Porous Cmc in Hypersonic Flow. In Proceedings of the 17th AIAA International Space Planes and Hypersonic Systems and Technologies Conference, San Francisco, CA, USA, 11–14 April 2011; pp. 1–13. [[CrossRef](#)]
34. Langener, T.; Von Wolfersdorf, J.; Steelant, J. Experimental Investigations on Transpiration Cooling for Scramjet Applications Using Different Coolants. *AIAA J.* **2011**, *49*, 1409–1419. [[CrossRef](#)]
35. Kumar, C.S.; Pattamatta, A. Assessment of Heat Transfer Enhancement Using Metallic Porous Foam Configurations in Laminar Slot Jet Impingement: An Experimental Study. *J. Heat Transfer* **2018**, *140*, 022202. [[CrossRef](#)]
36. Andrews, G.E.; Asere, A.A.; Mkpadi, M.C.; Tirmahi, A. Asme 1986 International Gas Turbine Conference Transpiration Cooling: Contribution of Film Cooling To the Overall Cooling Effectiveness. In Proceedings of the American Society of Mechanical Engineers (Paper), Dusseldorf, Germany, 8–12 June 1986; American Society of Mechanical Engineers: New York, NY, USA, 1986.
37. Polezhaev, J. The Transpiration Cooling for Blades of High Temperatures Gas Turbine. *Energy Convers. Manag.* **1997**, *38*, 1123–1133. [[CrossRef](#)]
38. Wang, Y.; Wang, L.; Zhou, Y.; Luo, Z.; Xie, W.; Liu, Q.; Peng, W.; Du, M. Research Progress on Transpiration Cooling Technology in Force-Thermal Concentrated Environments. *Int. J. Heat Mass Transf.* **2025**, *236*, 126262. [[CrossRef](#)]
39. Raj, R.; Moskowitz, S. *Transpiration Air Protected Turbine Blades—An Effective Concept To Achieve High Temperature and Erosion Resistance for Gas Turbines Operating in an Aggressive Environment*; American Society of Mechanical Engineers: New York, NY, USA, 1978; pp. 1–11.
40. Wadia, A.R. Advanced Combustor Linear Cooling Technology for Gas Turbines. *Def. Sci. J.* **1988**, *38*, 363–380. [[CrossRef](#)]
41. Bunker, R.S. *Gas Turbine Cooling: Moving from Macro to Micro Cooling*; American Society of Mechanical Engineers: New York, NY, USA, 2013; Volume 3C, pp. 1–17. [[CrossRef](#)]
42. Bunker, R.S. *Evolution of Turbine Cooling*; American Society of Mechanical Engineers: New York, NY, USA, 2017; Volume 1, pp. 1–26. [[CrossRef](#)]
43. Xu, L.; Sun, Z.; Ruan, Q.; Xi, L.; Gao, J.; Li, Y. Development Trend of Cooling Technology for Turbine Blades at Super-High Temperature of above 2000 K. *Energies* **2023**, *16*, 668. [[CrossRef](#)]

44. Mi, Q.; Yi, S.H.; Gang, D.D.; Lu, X.G.; Liu, X.L. Research Progress of Transpiration Cooling for Aircraft Thermal Protection. *Appl. Therm. Eng.* **2024**, *236*, 121360. [[CrossRef](#)]
45. Zhang, S.; Li, X.; Zuo, J.; Qin, J.; Cheng, K.; Feng, Y.; Bao, W. Research Progress on Active Thermal Protection for Hypersonic Vehicles. *Prog. Aerosp. Sci.* **2020**, *119*, 100646. [[CrossRef](#)]
46. Xu, R.; Cheng, Z.; Jiang, P. Fundamentals and Recent Progress of Additive Manufacturing-Assisted Porous Materials on Transpiration Cooling. *J. Glob. Power Propuls. Soc.* **2023**, *2023*, 19–48. [[CrossRef](#)]
47. Weinbaum, S.; Wheeler, H.L. Heat Transfer in Sweat-Cooled Porous Metals. *J. Appl. Phys.* **1949**, *20*, 113–122. [[CrossRef](#)]
48. Hald, H.; Ortelt, M.; Fischer, I.; Greuel, D. CMC Rocket Combustion Chamber with Effusion Cooling. In Proceedings of the 54th International Astronautical Congress of the International Astronautical Federation, the International Academy of Astronautics, and the International Institute of Space Law, Bremen, Germany, 29 September–3 October 2003; Volume 3, pp. 657–667. [[CrossRef](#)]
49. Huang, Z.; Xiong, Y.B.; Liu, Y.Q.; Jiang, P.X.; Zhu, Y.H. Experimental Investigation of Full-Coverage Effusion Cooling through Perforated Flat Plates. *Appl. Therm. Eng.* **2015**, *76*, 76–85. [[CrossRef](#)]
50. Wang, F.; Song, N.; Xia, X.; Chen, X. Experimental Investigation on Transpiration Cooling of Ammonium Carbonate in Porous Composite Structure at High-Temperature. *Appl. Therm. Eng.* **2024**, *249*, 123292. [[CrossRef](#)]
51. Huang, G.; Min, Z.; Yang, L.; Jiang, P.X.; Chyu, M. Transpiration Cooling for Additive Manufactured Porous Plates with Partition Walls. *Int. J. Heat Mass Transf.* **2018**, *124*, 1076–1087. [[CrossRef](#)]
52. Van Foreest, A.; Sippel, M.; Güllhan, A.; Esser, B.; Ambrosius, B.A.C.; Sudmeijer, K. Transpiration Cooling Using Liquid Water. *J. Thermophys. Heat Transf.* **2009**, *23*, 693–702. [[CrossRef](#)]
53. Liu, Y.; Liu, T.; Ding, R.; He, F.; Wang, J. Experimental and Numerical Investigation of Transpiration Cooling with Gradient Porosity Layout for the Thermal Protection of Nose Cone. *Aerospace Sci. Technol.* **2024**, *149*, 109140. [[CrossRef](#)]
54. Huang, G.; Zhu, Y.; Liao, Z.; Ouyang, X.L.; Jiang, P.X. Experimental Investigation of Transpiration Cooling with Phase Change for Sintered Porous Plates. *Int. J. Heat Mass Transf.* **2017**, *114*, 1201–1213. [[CrossRef](#)]
55. Glass, D.E. Ceramic Matrix Composite (CMC) Thermal Protection Systems (TPS) and Hot Structures for Hypersonic Vehicles. In Proceedings of the 15th AIAA International Space Planes and Hypersonic Systems and Technologies Conference, Dayton, Ohio, 28 April–1 May 2008; pp. 1–36. [[CrossRef](#)]
56. Xu, G.; Liu, Y.; Luo, X.; Ma, J.; Li, H. Experimental Investigation of Transpiration Cooling for Sintered Woven Wire Mesh Structures. *Int. J. Heat Mass Transf.* **2015**, *91*, 898–907. [[CrossRef](#)]
57. Gavaldà Diaz, O.; García Luna, G.; Liao, Z.; Axinte, D. The New Challenges of Machining Ceramic Matrix Composites (CMCs): Review of Surface Integrity. *Int. J. Mach. Tools Manuf.* **2019**, *139*, 24–36. [[CrossRef](#)]
58. Ekkad, S.V.; Zapata, D.; Han, J.C. Film Effectiveness over a Flat Surface with Air and CO₂ Injection through Compound Angle Holes Using a Transient Liquid Crystal Image Method. In Proceedings of the ASME 1995 International Gas Turbine and Aeroengine Congress and Exposition, Houston, TX, USA, 5–8 June 1995; p. 4. [[CrossRef](#)]
59. Blakey-Milner, B.; Gradl, P.; Snedden, G.; Brooks, M.; Pitot, J.; Lopez, E.; Leary, M.; Berto, F.; du Plessis, A. Metal Additive Manufacturing in Aerospace: A Review. *Mater. Des.* **2021**, *209*, 110008. [[CrossRef](#)]
60. Kamal, M.; Rizza, G. Design for Metal Additive Manufacturing for Aerospace Applications. In *Additive Manufacturing for the Aerospace Industry*; Elsevier Inc.: Amsterdam, The Netherlands, 2019; pp. 67–86, ISBN 9780128140635.
61. Najmon, J.C.; Raeisi, S.; Tovar, A. Review of Additive Manufacturing Technologies and Applications in the Aerospace Industry. In *Additive Manufacturing for the Aerospace Industry*; Elsevier Inc.: Amsterdam, The Netherlands, 2019; pp. 7–31, ISBN 9780128140635.
62. Tian, X.; Ye, W.; Xu, L.; Yang, A.; Huang, L.; Jin, S. Optimization Research on Laminated Cooling Structure for Gas Turbines: A Review. *AIMS Energy* **2025**, *13*, 354–401. [[CrossRef](#)]
63. Li, R.; Liu, J.; Shi, Y.; Du, M.; Xie, Z. 316L Stainless Steel with Gradient Porosity Fabricated by Selective Laser Melting. *J. Mater. Eng. Perform.* **2010**, *19*, 666–671. [[CrossRef](#)]
64. Cheng, Z.; Xu, R.; Jiang, P. Transpiration Cooling with Phase Change by Functionally Graded Porous Media. *Int. J. Heat Mass Transf.* **2023**, *205*, 123862. [[CrossRef](#)]
65. Nguyentat, T.; Hayes, W.A.; Meland, T.O.; Veith, E.M.; Ellis, D.L. Fabrication of a Liquid Rocket Combustion Chamber Liner of Advanced Copper Alloy GRCop-84 via Formed Platelet Liner Technology. In Proceedings of the 42nd AIAA/ASME/SAE/ASEE Joint Propulsion Conference & Exhibit, Sacramento, CA, USA, 9–12 July 2006; Volume 10, pp. 8335–8344. [[CrossRef](#)]
66. Traub, H.; Kube, J.; Jose, S.; Prasannakumar, A.; Hühne, C. Structural and Aerodynamic Characteristics of Micro-Perforated Porous Sheets for Laminar Flow Control. In Proceedings of the ASME 2024 Aerospace Structures, Structural Dynamics, and Materials Conference, SSDM 2024, Renton, WA, USA, 29 April–1 May 2024; American Society of Mechanical Engineers: New York, NY, USA, 2024; pp. 1–10.
67. Yeranee, K.; Rao, Y.; Zuo, Q.; Xie, J. Thermal Performance Enhancement for Gas Turbine Blade Trailing Edge Cooling with Topology-Optimized Printable Diamond TPMS Lattice. *Int. J. Heat Fluid Flow* **2024**, *110*, 109649. [[CrossRef](#)]

68. Sinha, A.; Swain, B.; Behera, A.; Mallick, P.; Samal, S.K.; Vishwanatha, H.M.; Behera, A. A Review on the Processing of Aero-Turbine Blade Using 3D Print Techniques. *J. Manuf. Mater. Process.* **2022**, *6*, 16. [[CrossRef](#)]
69. Kaur, I.; Aider, Y.; Nithyanandam, K.; Singh, P. Thermal-Hydraulic Performance of Additively Manufactured Lattices for Gas Turbine Blade Trailing Edge Cooling. *Appl. Therm. Eng.* **2022**, *211*, 118461. [[CrossRef](#)]
70. Wilson, J.M.; Piya, C.; Shin, Y.C.; Zhao, F.; Ramani, K. Remanufacturing of Turbine Blades by Laser Direct Deposition with Its Energy and Environmental Impact Analysis. *J. Clean. Prod.* **2014**, *80*, 170–178. [[CrossRef](#)]
71. Kaplanskii, Y.Y.; Levashov, E.A.; Korotitskiy, A.V.; Loginov, P.A.; Sentyurina, Z.A.; Mazalov, A.B. Influence of Aging and HIP Treatment on the Structure and Properties of NiAl-Based Turbine Blades Manufactured by Laser Powder Bed Fusion. *Addit. Manuf.* **2020**, *31*, 100999. [[CrossRef](#)]
72. Yang, T.; Mazumder, S.; Jin, Y.; Squires, B.; Sofield, M.; Pantawane, M.V.; Dahotre, N.B.; Neogi, A. A Review of Diagnostics Methodologies for Metal Additive Manufacturing Processes and Products. *Materials* **2021**, *14*, 4929. [[CrossRef](#)]
73. Kim, M.; Shin, D.H.; Kim, J.S.; Lee, B.J.; Lee, J. Experimental Investigation of Effusion and Transpiration Air Cooling for Single Turbine Blade. *Appl. Therm. Eng.* **2021**, *182*, 116156. [[CrossRef](#)]
74. Poupinha, C.; Kozlowska, S.; Lluch, J.S.; Altimate, D.; Kinell, M. Experimental Study on Transpiration Cooling through Additively Manufactured Porous Structures. *Int. J. Heat Mass Transf.* **2024**, *227*, 125532. [[CrossRef](#)]
75. Fantozzi, G.; Kinell, M.; Carrera, S.R.; Nilsson, J.; Kuesters, Y. Experimental Study on Pressure Losses in Porous Materials. In Proceedings of the ASME Turbo Expo, Oslo, Norway, 11–15 June 2018; American Society of Mechanical Engineers: New York, NY, USA, 2018; Volume 5B-2018, p. V05BT21A001.
76. Min, Z.; Huang, G.; Parbat, S.N.; Yang, L.; Chyu, M.K. Experimental Investigation on Additively Manufactured Transpiration and Film Cooling Structures. *J. Turbomach.* **2019**, *141*, 1–10. [[CrossRef](#)]
77. Min, Z.; Parbat, S.N.; Yang, L.; Chyu, M.K. Thermal-Fluid and Mechanical Investigations of Additively Manufactured Geometries for Transpiration Cooling. In Proceedings of the ASME Turbo Expo 2019: Turbomachinery Technical Conference and Exposition, Phoenix, AZ, USA, 17–21 June 2019; Volume 5B-2019, pp. 1–13. [[CrossRef](#)]
78. Chyu, M.; Kang, B.; Parbat, S. *Integrated Transpiration and Lattice Cooling Systems Developed by Additive Manufacturing with Oxide-Dispersion-Strengthened (ODS) Alloys*; National Energy Technology Laboratory: Pittsburgh, PA, USA, 2022.
79. Ealy, B.; Calderon, L.; Wang, W.; Valentin, R.; Mingareev, I.; Richardson, M.; Kapat, J. Characterization of Laser Additive Manufacturing-Fabricated Porous Superalloys for Turbine Components. *J. Eng. Gas Turbines Power* **2017**, *139*, 102102. [[CrossRef](#)]
80. Zhang, K.; Hickey, J.P.; Vlasea, M. An Analysis Framework of Additively Manufactured Deterministic Porous Structures for Transpiration Cooling. *J. Mater. Eng. Perform.* **2023**, *32*, 9253–9262. [[CrossRef](#)]
81. Son, J.; Broumand, M.; Pyo, Y.; Richer, P.; Jodoin, B.; Hong, Z. Effects of Lattice Orientation Angle on Tpms-Based Transpiration Cooling. In Proceedings of the ASME Turbo Expo 2024: Turbomachinery Technical Conference and Exposition, London, UK, 24–28 June 2024; Volume 13, pp. 1–13. [[CrossRef](#)]
82. Zhou, Z.; Lv, Y.; He, F.; Liu, T.; Wang, J. Pore-Scale Investigation of Transpiration Cooling Based on Triply Periodic Minimal Surface. *Int. J. Therm. Sci.* **2024**, *201*, 109019. [[CrossRef](#)]
83. Huang, G.; Zhu, Y.; Liao, Z.; Xu, R.; Jiang, P.X. Biomimetic Self-Pumping Transpiration Cooling for Additive Manufactured Porous Module with Tree-like Micro-Channel. *Int. J. Heat Mass Transf.* **2019**, *131*, 403–410. [[CrossRef](#)]
84. Yeranee, K.; Rao, Y. A Review of Recent Investigations on Flow and Heat Transfer Enhancement in Cooling Channels Embedded with Triply Periodic Minimal Surfaces (TPMS). *Energies* **2022**, *15*, 8994. [[CrossRef](#)]
85. Nield, D.A.; Bejan, A. *Convection in Porous Media*; Springer: Cham, Switzerland, 2017; Volume 165, ISBN 978-3-319-49561-3.
86. Wolf, J.; Moskowitz, S. Development of the Transpiration Air-Cooled Turbine for High-Temperature Dirty Gas Streams. *J. Eng. Power* **1983**, *105*, 821–825. [[CrossRef](#)]
87. Cheng, Z.; Xu, R.; Jiang, P.X. Morphology, Flow and Heat Transfer in Triply Periodic Minimal Surface Based Porous Structures. *Int. J. Heat Mass Transf.* **2021**, *170*, 120902. [[CrossRef](#)]
88. Cheng, Z.; Li, X.; Xu, R.; Jiang, P. Investigations on Porous Media Customized by Triply Periodic Minimal Surface: Heat Transfer Correlations and Strength Performance. *Int. Commun. Heat Mass Transf.* **2021**, *129*, 105713. [[CrossRef](#)]
89. Sun, H.; Ma, H.; Yan, L.; Fu, H.; Luan, Y.; Zunino, P. Numerical Simulations on the Performance of Transpiration Cooling Implemented with Perforated Flat Plates. *Appl. Therm. Eng.* **2024**, *238*, 121943. [[CrossRef](#)]
90. Liu, T.; He, F.; Wu, X.; Zhou, Z.; He, Y.; Wang, J. Numerical Investigation and Multi-Objective Structure Optimization of Transpiration Cooling on the Leading Edge of Turbine Blade. In Proceedings of the ASME Turbo Expo 2024: Turbomachinery Technical Conference and Exposition, London, UK, 24–28 June 2024; Volume 7, pp. 1–11. [[CrossRef](#)]
91. Zheng, J.; Liu, X.; Zhou, W.; Bian, Y. Numerical Investigation on Directional Transpiration Cooling Performance Coupled with Regenerative Cooling. *Int. Commun. Heat Mass Transf.* **2024**, *159*, 108223. [[CrossRef](#)]
92. Broumand, M.; Son, J.; Pyo, Y.; Yun, S.; Hong, Z. TPMS-Based Transpiration Cooling for Film Cooling Enhancement. *Int. J. Heat Mass Transf.* **2024**, *231*, 125824. [[CrossRef](#)]

93. Kumar, S.; Singh, O. Thermodynamic Performance Evaluation of Gas Turbine Cycle with Transpiration Cooling of Blades Using Air Vis-à-Vis Steam. *Proc. Inst. Mech. Eng. Part A J. Power Energy* **2010**, *224*, 1039–1047. [[CrossRef](#)]
94. Shukla, A.K.; Sharma, M.; Singh, O. Thermodynamic Investigation of Transpiration Cooled Gas Turbine Blade. In *Ergonomics for Improved Productivity*; Springer: Singapore, 2022; Volume 2, pp. 59–69, ISBN 9789380043487.
95. Kim, M.; Shin, D.H.; Lee, B.J.; Lee, J. Flow Characterization of Microscale Effusion and Transpiration Air Cooling on Single Blade. *Case Stud. Therm. Eng.* **2022**, *31*, 101863. [[CrossRef](#)]
96. Calderon, L.; Curbelo, A.; Gupta, G.; Kapat, J.S. Adiabatic Film Cooling Effectiveness of a Lam Fabricated Porous Leading Edge Segment of a Turbine Blade. In Proceedings of the ASME Turbo Expo 2018: Turbomachinery Technical Conference and Exposition, Oslo, Norway, 11–15 June 2018; Volume 5B-2018, pp. 1–9. [[CrossRef](#)]
97. Wambersie, A.; Wong, H.; Ireland, P.; Mayo, I. Experiments of Transpiration Cooling Inspired Panel Cooling on a Turbine Blade Yielding Film Effectiveness Levels over 95%. *Int. J. Turbomachinery, Propuls. Power* **2021**, *6*, 16. [[CrossRef](#)]
98. Aly, O.D.; Wright, L.M.; Hassan, I. Effect of Blowing Ratio on the Film Cooling Effectiveness on a Flat Plate with Various Blockage Ratios. In Proceedings of the ASME 2024 Heat Transfer Summer Conference; American Society of Mechanical Engineers, Anaheim, CA, USA, 15 July 2024; pp. 1–11.
99. Min, Z.; Parbat, S.; Wang, Q.M.; Chyu, M.K. Surface Heater Fabrication Using Micro-Lithography for Transpiration Cooling Heat Transfer Coefficient Measurements. *J. Turbomach.* **2022**, *144*, 071003. [[CrossRef](#)]
100. Fier, N.D.; Bogard, D.G. Additively Manufactured Porous Geometries for Hybrid Turbine Cooling. In Proceedings of the ASME Turbo Expo 2021: Turbomachinery Technical Conference and Exposition, Virtual, 7–11 June 2021; Volume 5A-2021, pp. 1–10. [[CrossRef](#)]
101. Brimacombe, B.J.; Scobie, J.A.; Flynn, J.M.; Sangan, C.M.; Pountney, O.J. Effect of Porosity and Injection Ratio on the Performance of Transpiration Cooling through Gyroids. *Int. J. Turbomachinery, Propuls. Power* **2023**, *8*, 50. [[CrossRef](#)]
102. Son, J.; Pyo, Y.; Richer, P.; Jodoin, B.; Hong, Z. Impact of TPMS Structure Unit Cell Size on Transpiration Cooling. In Proceedings of the AIAA Science and Technology Forum and Exposition, AIAA SciTech Forum 2025, Orlando, FL, USA, 10 October 2024–6 January 2025; pp. 1–17.
103. Zhang, L.; Zhang, Y.; Sun, J.; Xu, G.; Wen, J. Model and Simulation of Two-Phase Transpiration Cooling Process for Aero-Engine Thermal Protection. In *Asia-Pacific International Symposium on Aerospace Technology*; Lecture Notes in Electrical Engineering; Springer: Singapore, 2024; Volume 1051 LNEE, pp. 1047–1062, ISBN 9789819740093.
104. Ngetich, G.C.; Ireland, P.T.; Romero, E. Study of Film Cooling Effectiveness on a Double-Walled Effusion-Cooled Turbine Blade in a High-Speed Flow Using Pressure Sensitive Paint. In Proceedings of the ASME Turbo Expo 2019: Turbomachinery Technical Conference and Exposition, Phoenix, AZ, USA, 17–21 June 2019; Volume 5B-2019, pp. 1–14. [[CrossRef](#)]
105. Meng, T.; Zhu, H.; Liu, C.; Yu, Q.; Wei, J. Accuracy of Superposition Predictions of Film Cooling Effectiveness on a Flat Plate with Double Rows of Holes. In Proceedings of the Volume 5C: Heat Transfer; American Society of Mechanical Engineers, Seoul, Republic of Korea, 13 June 2016; Volume 56865, pp. 1–10.
106. Son, J.; Pyo, Y.; Broumand, M.; Hong, Z.; Sarafan, S.; Wanjara, P. Advanced Transpiration Cooling Method Using Additive Manufactured TPMS Structure. In *Proceedings of the 62nd Conference of Metallurgists, COM 2023*; Springer: Cham, Switzerland, 2023; pp. 449–451, ISBN 9783031381409.
107. Chao-Yang, W.; Beckermann, C. A Two-Phase Mixture Model of Liquid-Gas Flow and Heat Transfer in Capillary Porous Media-I. Formulation. *Int. J. Heat Mass Transf.* **1993**, *36*, 2747–2758. [[CrossRef](#)]
108. Ergun, S.; Orning, A.A. Fluid Flow through Randomly Packed Columns and Fluidized Beds. *Ind. Eng. Chem.* **1949**, *41*, 1179–1184. [[CrossRef](#)]
109. Shen, B.X.; Liu, W.Q. Effect of Hot Fuel Gas on a Combinational Opposing Jet and Platelet Transpiration Thermal Protection System. *Appl. Therm. Eng.* **2020**, *164*, 114513. [[CrossRef](#)]
110. Wang, X.; Fan, X.; Xiong, B. Numerical Study of Transpiration Cooling at Different Outlet Angles and Hole Pattern. *Int. J. Heat Fluid Flow* **2024**, *109*, 109551. [[CrossRef](#)]
111. Yang, L.; Min, Z.; Parbat, S.N.; Chyu, M.K. Effect of Pore Blockage on Transpiration Cooling with Additive Manufacturable Perforate Holes. In Proceedings of the ASME Turbo Expo 2018: Turbomachinery Technical Conference and Exposition, Oslo, Norway, 11–15 June 2018; Volume 2D-2018, pp. 1–9. [[CrossRef](#)]
112. Yang, L.; Chen, W.; Chyu, M.K. A Convolution Modeling Method for Pore Plugging Impact on Transpiration Cooling Configurations Perforated by Straight Holes. *Int. J. Heat Mass Transf.* **2018**, *126*, 1057–1066. [[CrossRef](#)]
113. Sun, H.; Ma, H.; Yan, L.; Fu, H.; Luan, Y.; Magagnato, F. Effect of Pore Blockage on Transpiration Cooling of Marine Turbine Blades. In *International Conference on Marine Equipment & Technology and Sustainable Development*; Lecture Notes in Civil Engineering; Springer: Singapore, 2023; Volume 375 LNCE, pp. 631–649, ISBN 9789819942909.
114. Yang, Y.; Zhang, B.; Fan, X.; Zhao, R. Numerical Investigation on Transpiration Cooling Performance of Oriented Porous Structure Under Local Block Conditions. *J. Thermophys. Heat Transf.* **2024**, *38*, 311–320. [[CrossRef](#)]
115. Huang, G.; He, L. Influence of Inhomogeneous Porosity on Effusion Cooling. *Int. J. Heat Mass Transf.* **2019**, *144*, 118675. [[CrossRef](#)]

116. Yang, Y.; Mao, J.; Chen, P.; Zhang, H.; Tang, H. Numerical Investigation on Transpiration Cooling Performance with Different Porosities and Mainstream Pressure Gradients. *Int. J. Therm. Sci.* **2023**, *184*, 107991. [[CrossRef](#)]
117. Li, H.; Xie, F.; Zhuang, Y.; Wang, Y.; Yan, Y.; Xu, G.; Cui, J. Numerical Investigation of Cooling Performance of 3D-Printable Cooling Structure for Aero-Engine Combustor. *Appl. Therm. Eng.* **2024**, *238*, 122196. [[CrossRef](#)]
118. Purnadiana, F.R.; Prabowo; Sasongko, H. The Performance Comparison Between Modelled and Fully Simulated Porous Media in Turbine Blade Cooling. In *International Conference on Mechanical Engineering*; Springer: Singapore, 2025; pp. 31–38; ISBN 9789819781966.
119. Nisar, F.; Rojek, J.; Nosewicz, S.; Kaszyca, K.; Chmielewski, M. Evaluation of Effective Thermal Conductivity of Sintered Porous Materials Using an Improved Discrete Element Model. *Powder Technol.* **2024**, *437*, 119546. [[CrossRef](#)]
120. Yang, L.; Min, Z.; Yue, T.; Rao, Y.; Chyu, M.K. High Resolution Cooling Effectiveness Reconstruction of Transpiration Cooling Using Convolution Modeling Method. *Int. J. Heat Mass Transf.* **2019**, *133*, 1134–1144. [[CrossRef](#)]
121. Yang, L.; Dai, W.; Rao, Y.; Chyu, M.K. A Machine Learning Approach to Quantify the Film Cooling Superposition Effect for Effusion Cooling Structures. *Int. J. Therm. Sci.* **2021**, *162*, 106774. [[CrossRef](#)]
122. Wang, W.; Tao, G.; Ke, D.; Luo, J.; Cui, J. Transpiration Cooling of High Pressure Turbine Vane with Optimized Porosity Distribution. *Appl. Therm. Eng.* **2023**, *223*, 119831. [[CrossRef](#)]
123. Wang, W.; Tao, G.; Ke, D.; Ruan, Z.; Liu, J.; Luo, J.; Cui, J. Multi-Objective Optimization of Transpiration Cooling for High Pressure Turbine Vane. *Appl. Therm. Eng.* **2024**, *246*, 122926. [[CrossRef](#)]
124. Chen, W.; Wang, K.; Wang, Y.; Tu, S.; Liu, Z.; Su, H. Numerical Investigation and Optimal Design of Transpiration Cooling Plate Structure for Gradient Porosity. *Int. J. Therm. Sci.* **2024**, *197*, 108755. [[CrossRef](#)]
125. Min, Z.; Wu, Y.; Yang, K.; Xu, J.; Parbat, S.N.; Chyu, M.K. Dimensional Characterizations Using Scanning Electron Microscope and Surface Improvement with Electrochemical Polishing of Additively Manufactured Microchannels. *J. Eng. Gas Turbines Power* **2021**, *143*, 041020. [[CrossRef](#)]
126. Carneiro, V.H.; Rawson, S.D.; Puga, H.; Meireles, J.; Withers, P.J. Additive Manufacturing Assisted Investment Casting: A Low-Cost Method to Fabricate Periodic Metallic Cellular Lattices. *Addit. Manuf.* **2020**, *33*, 101085. [[CrossRef](#)]
127. Al-Ketan, O.; Singh, A.; Karathanasopoulos, N. Strut and Sheet Metal Lattices Produced via AM-Assisted Casting and Powder Bed Fusion: A Comparative Study. *Addit. Manuf. Lett.* **2023**, *4*, 100118. [[CrossRef](#)]
128. Zocca, A.; Colombo, P.; Gomes, C.M.; Günster, J. Additive Manufacturing of Ceramics: Issues, Potentialities, and Opportunities. *J. Am. Ceram. Soc.* **2015**, *98*, 1983–2001. [[CrossRef](#)]
129. Li, H.; Liu, Y.; Liu, Y.; Zeng, Q.; Wang, J.; Hu, K.; Lu, Z.; Liang, J. Evolution of the Microstructure and Mechanical Properties of Stereolithography Formed Alumina Cores Sintered in Vacuum. *J. Eur. Ceram. Soc.* **2020**, *40*, 4825–4836. [[CrossRef](#)]
130. An, X.; Mu, Y.; Liang, J.; Li, J.; Zhou, Y.; Sun, X. Stereolithography 3D Printing of Ceramic Cores for Hollow Aeroengine Turbine Blades. *J. Mater. Sci. Technol.* **2022**, *127*, 177–182. [[CrossRef](#)]
131. Min, Z.; Parbat, S.N.; Yang, L.; Kang, B.; Chyu, M.K. Fabrication and Characterization of Additive Manufactured Nickel-Based Oxide Dispersion Strengthened Coating Layer for High-Temperature Application. *J. Eng. Gas Turbines Power* **2018**, *140*, 062101. [[CrossRef](#)]
132. Ding, R.; Wang, J.; He, F.; Dong, G.; Tang, L. Numerical Investigation on the Performances of Porous Matrix with Transpiration and Film Cooling. *Appl. Therm. Eng.* **2019**, *146*, 422–431. [[CrossRef](#)]
133. Natsui, G.; Johnson, P.L.; Torrance, M.C.; Ricklick, M.A.; Kapat, J.S. The Effect of Transpiration on Discrete Injection for Film Cooling. In Proceedings of the ASME Turbo Expo, ASMEDC, Vancouver, BC, Canada, 1 January 2011; Volume 5, pp. 509–520.
134. Lv, Y.; Liu, L.; Ma, Y.; Dou, Y.; He, F.; Wang, J. Experimental Investigation on Cooling Characteristic of Transpiration-Film Combined Cooling Structure Using Liquid Coolant. *Int. Commun. Heat Mass Transf.* **2024**, *158*, 107964. [[CrossRef](#)]
135. Supar, K.; Ahmad, H. Stress Distribution Study on Multi-Holes Configurations in Woven Fabric Kenaf Composite Plates. *IOP Conf. Ser. Mater. Sci. Eng.* **2017**, *271*, 012005. [[CrossRef](#)]
136. Ligrani, P.M.; Bueschges, C.; Tatge, M.; Weigand, B.; Subramanian, C.; Collopy, H.L.; Taylor, Z.; Sheth, J.; Gradl, P. Heat Transfer and Aerodynamic Losses of Additively Manufactured Turbine Alloy Blades with Different Surface Enhancement Post-Processing. *Int. J. Therm. Sci.* **2025**, *214*, 109914. [[CrossRef](#)]
137. Arai, M.; Suidzu, T. Porous Ceramic Coating for Transpiration Cooling of Gas Turbine Blade. *J. Therm. Spray Technol.* **2013**, *22*, 690–698. [[CrossRef](#)]
138. Xiao, X.; Zhao, G.; Zhou, W.; Martynenko, S. Large-Eddy Simulation of Transpiration Cooling in Turbulent Channel with Porous Wall. *Appl. Therm. Eng.* **2018**, *145*, 618–629. [[CrossRef](#)]
139. You, R.; Liu, Z.; Wang, Q.; Li, H. Study on the Flow and Heat Transfer Characteristics of a Double-Wall Structure with Multiple-Jet Impingement Cooling under Rotating Conditions. *Int. Commun. Heat Mass Transf.* **2025**, *161*, 108299. [[CrossRef](#)]
140. Zhang, W.; Yi, Y.; Bai, X.; Nakayama, A. A Local Thermal Non-Equilibrium Analysis for Convective and Radiative Heat Transfer in Gaseous Transpiration Cooling through a Porous Wall. *Int. J. Heat Mass Transf.* **2020**, *162*, 120389. [[CrossRef](#)]

141. Munk, D.J.; Selzer, M.; Steven, G.P.; Vio, G.A. Topology Optimization Applied to Transpiration Cooling. *AIAA J.* **2019**, *57*, 297–312. [[CrossRef](#)]
142. Jiang, Y.; Hu, J.; Wang, S.; Lei, N.; Luo, Z.; Liu, L. Meshless Optimization of Triply Periodic Minimal Surface Based Two-Fluid Heat Exchanger. *CAD Comput. Aided Des.* **2023**, *162*, 103554. [[CrossRef](#)]

Disclaimer/Publisher’s Note: The statements, opinions and data contained in all publications are solely those of the individual author(s) and contributor(s) and not of MDPI and/or the editor(s). MDPI and/or the editor(s) disclaim responsibility for any injury to people or property resulting from any ideas, methods, instructions or products referred to in the content.